

Near-Ultraviolet Photodissociation of Thiophenol<sup>†</sup>

Adam L. Devine, Michael G. D. Nix, Richard N. Dixon, and Michael N. R. Ashfold\*

School of Chemistry, University of Bristol, Bristol BS8 1TS, U.K.

Received: March 7, 2008; Revised Manuscript Received: April 28, 2008

H(D) Rydberg atom photofragment translational spectroscopy has been used to investigate the dynamics of H(D) atom loss  $\text{C}_6\text{H}_5\text{SH}(\text{C}_6\text{H}_5\text{SD})$  following excitation at many wavelengths  $\lambda_{\text{phot}}$  in the range of 225–290 nm. The  $\text{C}_6\text{H}_5\text{S}$  cofragments are formed in both their ground ( $\text{X}^2\text{B}_1$ ) and first excited ( $^2\text{B}_2$ ) electronic states, in a distribution of vibrational levels that spreads and shifts to higher internal energies as  $\lambda_{\text{phot}}$  is reduced. Excitation at  $\lambda_{\text{phot}} > 275$  nm populates levels of the first  $^1\pi\pi^*$  state, which decay by tunnelling to the dissociative  $^1\pi\sigma^*$  state potential energy surface (PES). S–H torsional motion is identified as a coupling mode facilitating population transfer at the conical intersection (CI) between the diabatic  $^1\pi\pi^*$  and  $^1\pi\sigma^*$  PESs. At shorter  $\lambda_{\text{phot}}$ , the  $^1\pi\sigma^*$  state is deduced to be populated either directly or by efficient vibronic coupling from higher  $^1\pi\pi^*$  states. Flux evolving on the  $^1\pi\sigma^*$  PES samples a second CI, at longer  $R_{\text{S-H}}$ , between the diabatic  $^1\pi\sigma^*$  and ground ( $^1\pi\pi$ ) PESs, where the electronic branching between ground and excited state  $\text{C}_6\text{H}_5\text{S}$  fragments is determined. The  $\text{C}_6\text{H}_5\text{S}(\text{X}^2\text{B}_1)$  and  $\text{C}_6\text{H}_5\text{S}(\text{X}^2\text{B}_2)$  products are deduced to be formed in levels with, respectively,  $a'$  and  $a''$  vibrational symmetry—behavior that reflects both Franck–Condon effects (both in the initial photoexcitation step and in the subsequent in-plane forces acting during dissociation) and the effects of the out-of-plane coupling mode(s),  $\nu_{11}$  and  $\nu_{16a}$ , at the  $^1\pi\sigma^*/^1\pi\pi$  CI. The vibrational state assignments enabled by the high-energy resolution of the present data allow new and improved estimations of the bond dissociation energies,  $D_0(\text{C}_6\text{H}_5\text{S-H}) \leq 28030 \pm 100 \text{ cm}^{-1}$  and  $D_0(\text{C}_6\text{H}_5\text{S-D}) \leq 28610 \pm 100 \text{ cm}^{-1}$ , and of the energy separation between the  $\text{X}^2\text{B}_1$  and  $^2\text{B}_2$  states of the  $\text{C}_6\text{H}_5\text{S}$  radical,  $T_{00} = 2800 \pm 40 \text{ cm}^{-1}$ . Similarities, and differences, between the measured energy disposals accompanying UV photoinduced X–H (X = S, O) bond fission in thiophenol and phenol are discussed.

## 1. Introduction

Predictions by Sobolewski and Domcke<sup>1</sup> regarding dissociative excited electronic states of  $^1\pi\sigma^*$  character in heteroaromatic molecules have fueled much recent interest in the photofragmentation behavior of these compounds.<sup>2</sup> Ab initio studies reveal the potential energy surfaces (PESs) of these  $^1\pi\sigma^*$  states to be repulsive in the X–H coordinate (where X is the heteroatom, for example, N, O, or, as here, S), leading to speculations regarding the possible importance of X–H fission in the nonradiative decay of these molecules following ultraviolet (UV) photoexcitation. Calculations<sup>3</sup> on first-row heteroaromatic molecules (e.g., phenol, pyrrole, indole) indicate that, in each case, the  $^1\pi\sigma^*$  states have 3s Rydberg character in the vertical Franck–Condon region and  $\sigma^*_{\text{X-H}}$  antibonding valence character at extended  $R_{\text{X-H}}$ . These  $^1\pi\sigma^*$  electronic states also exhibit low oscillator strengths from the ground state and large dipole moments. In phenol, the diabatic  $^1\pi\sigma^*$  PES was found to intersect both the bound, photobright, diabatic  $^1\pi\pi^*$  state and the ground state in the O–H stretch coordinate. [For clarity, we use the terms  $^1\pi\sigma^*$ ,  $^1\pi\pi^*$ ,  $^1\pi\pi$ , etc to label the diabatic states (and PESs) of interest, and reserve the descriptors  $S_0$ ,  $S_1$ , etc for the corresponding adiabatic states and PESs.] These crossing points develop into conical intersections (CIs) with out-of-plane distortion of the nuclear framework.<sup>4</sup>

We have presented a detailed study of the H atom loss dynamics following UV photolysis of phenol at many wavelengths in the range of  $200 \leq \lambda_{\text{phot}} \leq 280 \text{ nm}$ <sup>5</sup> using the H

atom photofragment translational spectroscopy (PTS) technique. The measured spectra provide information about the vibrational-state population distributions in the phenoxyl radical fragments formed upon O–H bond fission, which, in turn, provide insight into the nature of the coupling modes at the CIs between the  $^1\pi\sigma^*/^1\pi\pi^*$  and  $^1\pi\sigma^*/^1\pi\pi$  PESs in the O–H dissociation coordinate. To investigate the effect of the heteroatom identity in such heteroaromatics and to explore the generality of X–H fission via  $^1\pi\sigma^*$  states in second-row heteroaromatics, this article focuses on the H/D atom loss pathway following UV photodissociation of thiophenol- $h_1$  and thiophenol- $d_1$  ( $\text{C}_6\text{H}_5\text{SH}$  and  $\text{C}_6\text{H}_5\text{SD}$ ), the sulfur analogue of phenol.

Experimental<sup>6</sup> and theoretical<sup>7</sup> investigations indicate that the ground-state equilibrium structure of thiophenol is planar, and microwave studies<sup>8</sup> are consistent with a torsional barrier for rotation about the C–S bond of  $270 \text{ cm}^{-1}$ . An early PTS study<sup>9</sup> investigated C–S bond fission in  $\text{C}_6\text{H}_5\text{SH}$  (following excitation at 193 nm) and derived a value for the relevant bond dissociation energy,  $D_0(\text{C}_6\text{H}_5\text{-SH}) = 365 \pm 8 \text{ kJ mol}^{-1}$ . Ion imaging studies of  $\text{C}_6\text{H}_5\text{SH}$  (and  $\text{C}_6\text{H}_5\text{SD}$ ) photolysis at 243.1 nm revealed that the H/D fragments formed upon S–H(D) bond fission have bimodal translational energy distributions, attributable to thiophenoxyl radical formation in both the ground ( $\text{X}^2\text{B}_1$ ) and first excited ( $^2\text{B}_2$ ) electronic states.<sup>10,11</sup> Both dissociation channels exhibited anisotropic photofragment recoil velocity ( $\mathbf{v}$ ) distributions, with  $\mathbf{v}$  preferentially aligned perpendicular to the laser polarization axis, indicating prompt dissociation, relative to the time scale of molecular rotation. These authors also noted that since these two states of  $\text{C}_6\text{H}_5\text{S}$  differ only in the relative orientation of the singly occupied  $3p\pi$  orbital localized on the sulfur (parallel or perpendicular to the molecular plane), UV

<sup>†</sup> Part of the “Stephen R. Leone Festschrift”.

\* To whom correspondence should be addressed. Tel: (117)-9288312/3. Fax: (117)-9250612. E-mail: mike.ashfold@bris.ac.uk.

photolysis of  $\text{C}_6\text{H}_5\text{SH}$  represents a route to achieving intramolecular orbital alignment within this radical. In this article, we present a detailed study of the H/D atom loss pathway from  $\text{C}_6\text{H}_5\text{SH}/\text{C}_6\text{H}_5\text{SD}$  following photolysis at many wavelengths within the range of  $225 \leq \lambda_{\text{phot}} \leq 290$  nm. We also present complementary “action spectra” for forming H/D atoms, (monitored as  $\text{H}^+/\text{D}^+$  ions) as a function of  $\lambda_{\text{phot}}$ . The long-wavelength onset for H/D atom formation coincides with the onset of parent absorption at  $\sim 290$  nm, which we assign to the  $\text{S}_1 - \text{S}_0(\pi^* \leftarrow \pi)$  origin. A weak, structured, resonance-enhanced multiphoton ionization (REMPI) spectrum of the parent ion was also recorded. The long-wavelength onset of this spectrum was found to lie at slightly higher energy than the  ${}^1\pi\pi^*(\text{S}_1)$  origin; this we interpret in terms of absorption to, and subsequent ionization from, a longer lived triplet state.

The present H atom TOF spectra confirm the previous findings<sup>10,11</sup> regarding thiophenoxyl radical formation in both the ground and first excited electronic states, even at the long-wavelength absorption limit ( $\sim 290$  nm). Structure present in the TOF spectra indicates that these radicals are formed in a select subset of the available vibrational levels, the assignments of which provide detailed insights into the fragmentation mechanisms. Polarization dependence studies reveal that photolysis at  $\lambda_{\text{phot}} > 275$  nm results in an isotropic distribution of radical recoil velocities, whereas at shorter wavelengths, the fastest fragments are formed with perpendicular recoil anisotropy. Comparison between H and D atom TOF spectra obtained following photolysis of  $\text{C}_6\text{H}_5\text{SH}$  and  $\text{C}_6\text{H}_5\text{SD}$  reveals contributions from rival C–H bond fission processes to the measured photofragment yield at a given  $\lambda_{\text{phot}}$ , while comparisons between the present data and that reported recently for the related heteroaromatic system, phenol,<sup>4,5</sup> and the 4-halophenols<sup>12</sup> serve to highlight similarities and differences in the relative activities of different coupling modes at the CIs sampled en route to dissociation that are revealed in the eventual product state distributions.

## 2. Experimental Section

The experimental setup for the H/D (Rydberg) atom PTS studies has been described previously.<sup>13</sup> Thiophenol ( $\text{C}_6\text{H}_5\text{SH}$ ) was obtained commercially (Acros Organics,  $\geq 99\%$  purity). and its vapor pressure ( $\sim 2$  Torr) seeded in argon backing gas ( $\sim 700$  Torr) was expanded into vacuum through a pulsed valve (General Valve Series 9). Thiophenol- $d_1$  ( $\text{C}_6\text{H}_5\text{SD}$ ) was prepared by mixing  $\text{C}_6\text{H}_5\text{SH}$  (5 ml) with excess  $\text{D}_2\text{O}$  and shaking vigorously. The resulting  $\text{C}_6\text{H}_5\text{SD}$  was vacuum distilled into a glass bulb, which was subsequently filled with argon to a total pressure of 700 Torr, and the gas mixture was admitted to the vacuum system as described above.

Photolysis radiation was provided by the second-harmonic output of a Nd-YAG pumped dye laser (Spectra Physics GCR-270 plus PDL-2), which yielded UV pulse energies in the range of 0.5–3 mJ. This radiation was focused into the interaction region with a 75 cm focal length lens. The wavelength of the dye laser radiation was established by directing a fraction of the fundamental into a wavemeter (Coherent, Wavemaster). The polarization vector ( $\epsilon_{\text{phot}}$ ) could be aligned at any angle  $\theta$  relative to the TOF axis using a polarization rotator (Newport RFU double Fresnel rhomb). H/D atom TOF spectra were recorded with  $\epsilon_{\text{phot}}$  aligned at  $\theta = 0, 54.7$ , and  $90^\circ$  to the detection axis. The photolysis laser pulse was followed, after  $\sim 10$  ns, by the two pulses used for double-resonant excitation of the H/D atom photoproducts via their  $n = 2$  state to a Rydberg state with high principal quantum number ( $n \sim 80$ ). The requisite photons at

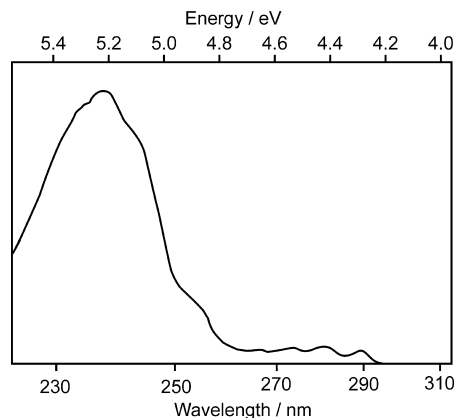


**Figure 1.** (a) UV absorption spectrum of  $\text{C}_6\text{H}_5\text{SH}$  recorded at 77 K, adapted from ref 17.

the Lyman- $\alpha$  wavelength ( $\lambda \sim 121.6$  nm,  $\nu = 82259$   $\text{cm}^{-1}$  ( $\text{H}_\alpha$ ) [ $\nu = 82280$   $\text{cm}^{-1}$  ( $\text{D}_\alpha$ )]) and at  $\lambda \sim 366$  nm were provided by two dye lasers pumped by a single Nd-YAG laser (Continuum Powerlite 9010). The Lyman- $\alpha$  radiation was generated by mixing the appropriate dye laser output with residual 1064 nm Nd-YAG laser fundamental output and then focussing the resulting linearly polarized 364.7 nm radiation into a phase-matched Kr/Ar mixture. The Lyman- $\alpha$  radiation so derived was then refocused ( $\text{MgF}_2$  lens) into the interaction volume situated 57 cm beyond the end of the tripling gas cell. The  $\lambda = 366$  nm photons required for the second step of the double-resonant excitation scheme were obtained by frequency doubling (in a DCDA crystal) 732 nm dye laser radiation.

The composition of the molecular beam was investigated by resonance-enhanced multiphoton ionization (REMPI) in the source region of a (removable) TOF mass spectrometer within the apparatus. REMPI spectra were obtained by scanning the photolysis laser in the range of  $225 \leq \lambda_{\text{phot}} \leq 295$  nm, monitoring the yield of parent ( $m/z$  110) ions. Introducing Lyman- $\alpha$  radiation and the 364.7 nm UV fundamental from which it is derived allowed measurement of action spectra for forming H/D atoms (detected as  $\text{H}^+/\text{D}^+$  ions following  $(1+1')$  resonance-enhanced threshold ionization).

The length of the TOF axis used in these experiments ( $d = 370$ – $371$  mm) was frequently recalibrated by recording TOF spectra of H/D atoms resulting from  $\text{H}_2\text{S}/\text{D}_2\text{S}$  photolysis at  $225 \leq \lambda_{\text{phot}} \leq 260$  nm and least-squares fitting to well-characterized peaks associated with the various H/D + SH/SD ( $X, \nu, N$ ) product channels<sup>14,15</sup> using literature values for  $D_0(\text{H}-\text{SH})$ ,  $D_0(\text{D}-\text{SD})$ , and the respective diatomic term values.<sup>16</sup>

## 3. Results and Discussion

### 3.1. Mass Spectroscopy and REMPI Excitation Studies.

Ion TOF mass spectra (MS) of  $\text{C}_6\text{H}_5\text{SH}$  were recorded at many wavelengths in the range of  $225 \leq \lambda_{\text{phot}} \leq 290$  nm using various laser pulse combinations and relative timings in order to gain insight into the various photofragmentation pathways. The 77 K electronic absorption spectrum of thiophenol (reproduced in Figure 1) shows the onset of UV absorption at  $\sim 34000$   $\text{cm}^{-1}$  (294 nm).<sup>17</sup> The ionization potential of thiophenol (8.30 eV<sup>18</sup>) lies below the two-photon energy at this wavelength, yet minimal parent ( $m/z$  110) ion signal was observed when exciting at any  $\lambda_{\text{phot}} > 284$  nm. As Figure 2a shows, a weak, structured parent ion spectrum with origin at  $\lambda_{\text{phot}} = 282.975$  nm ( $\tilde{\nu}_{00} = 35339$   $\text{cm}^{-1}$ ) was observed, however. The parent ion yield declined as  $\lambda_{\text{phot}}$  was reduced further, and by  $\lambda_{\text{phot}} = 265$  nm, little photolysis-laser-dependent  $m/z$  110 ion yield was observ-

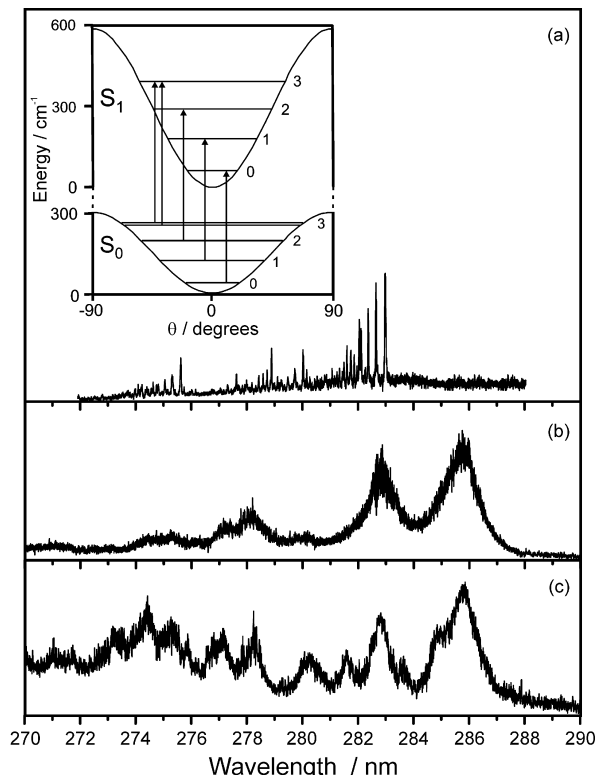


**Figure 2.** Excitation (or action) spectra for forming ions with (a)  $m/z$  110 (the parent ion mass) following one color multiphoton ionization of excitation of a jet-cooled sample of  $C_6H_5SH$ , (b)  $m/z$  1 ( $H^+$ ) following ionization of neutral H atom products arising in the one UV photon dissociation of  $C_6H_5SH$ , and (c)  $m/z$  2 ( $D^+$ ) from the corresponding UV photolysis of  $C_6H_5SD$ . The inset in (a) shows the calculated pattern of ground- and excited-state torsional levels and the  $\Delta\tau_{S-H} = 0$  transitions to which we attribute the observed fine structure.

able. The separations between the sharp peaks near this origin are  $\sim 40 \text{ cm}^{-1}$ . Such small peak spacings are most plausibly associated with torsional transitions of the S–H rotor. Calculations employing model  $V_2$  torsional potentials with respective barrier heights of  $300 \text{ cm}^{-1}$  for the  $S_0$  state (cf. an experimental estimate of  $\sim 267 \text{ cm}^{-1}$  (ref 8)) and  $590 \text{ cm}^{-1}$  for the excited state (illustrated in the inset to Figure 2a) reproduce the observed structure satisfactorily and show that these features are associated with  $\Delta\tau_{S-H} = 0$  transitions from ground-state levels, with  $\tau_{S-H} = 0, 1, 2, 3, \dots$ . The calculations succeed in reproducing the evident splitting of the fourth peak (attributable to tunneling splitting of the  $3a_1$  and  $3a_2$  torsional components of the  $\tau_{S-H} = 3$  level in the  $S_0$  state) but require the assumption of a torsional temperature of  $\sim 300 \text{ K}$  within the  $S_0$  state in order to replicate the observed intensity distribution. It is currently unclear why this torsional mode should cool so inefficiently in our molecular beam expansion. [The first ( $\tau_1^+$ ) member of the corresponding torsional progression was observed, weakly, in the action spectra for forming both parent ions and H atom products in previous studies of phenol in this same apparatus,<sup>5</sup> but the torsional level spacing in that case is much larger ( $\tau_{O-H} = 309 \text{ cm}^{-1}$ )]. A room-temperature Boltzmann distribution over the deduced torsional levels of  $C_6H_5SH(S_0)$  yields an average internal energy of  $\langle E_{\text{int}}(C_6H_5SH) \rangle \sim 100 \text{ cm}^{-1}$ . The structure evident in the range of  $281 \leq \lambda_{\text{phot}} \leq 282.975 \text{ nm}$  repeats at higher wavenumbers, most notably at  $\tilde{\nu}_{00} + 372 \text{ cm}^{-1}$ ,  $\tilde{\nu}_{00} + 682 \text{ cm}^{-1}$ , and  $\tilde{\nu}_{00} + 946 \text{ cm}^{-1}$ . This we attribute to analogous torsional progressions, built off of different vibrational levels within the excited electronic state. This parent ion yield is presumed to arise as a result of  $1 + 1$  REMPI via a relatively long-lived state with

**TABLE 1: Vertical Excitation Energies of (and Oscillator Strengths to) the first few Singlet and Triplet Excited States of  $C_6H_5SH$ , Calculated at the Ground-State Equilibrium Geometry at the TD-DFT HCTH/6-311G++(d,p) Level**

state	excitation energy / eV	wavelength / nm	state symmetry	nature of excitation	oscillator strength
T <sub>1</sub>	3.59	345	A'	$\pi \rightarrow \pi^*$	N/A
T <sub>2</sub>	3.82	324	A'	$\pi \rightarrow \pi^*$	N/A
T <sub>3</sub>	4.35	285	A''	$\pi \rightarrow \sigma^*$	N/A
S <sub>1</sub>	4.36	285	A'	$\pi \rightarrow \pi^*$	0.009
T <sub>4</sub>	4.37	283	A'	$\pi \rightarrow \pi^*$	N/A
S <sub>2</sub>	4.52	274	A''	$\pi \rightarrow \sigma^*$	0.003
S <sub>3</sub>	4.89	254	A'	$\pi \rightarrow \pi^*$	0.250
T <sub>5</sub>	4.90	253	A'	$\pi \rightarrow \pi^*$	N/A
T <sub>6</sub>	5.10	243	A''	$\pi \rightarrow \sigma^*$	N/A
S <sub>4</sub>	5.17	240	A''	$\pi \rightarrow \sigma^*$	0.002

small oscillator strength, possibly a triplet state. Similar studies of the  $C_6H_5SD$  isotopologue failed to identify any corresponding wavelength-dependent parent ion yield.

The Lyman- $\alpha$  radiation (together with the 364.7 nm precursor radiation from which it is derived) alone also yielded a weak parent ( $m/z$  110) ion signal but negligible  $H^+$  or other parent ion fragmentation products. However, TOF-MS recorded with both the photolysis and Lyman- $\alpha$  pulses present, with the latter delayed by  $\sim 10 \text{ ns}$ , showed a dominant  $H^+$  ion signal. Two-color excitation spectra for forming  $H^+/D^+$  ions from  $C_6H_5SH/C_6H_5SD$  were recorded across the range of  $240 \leq \lambda_{\text{phot}} \leq 295 \text{ nm}$ . As shown in Figure 2b and c, both spectra exhibit a number of broad features and very similar long-wavelength onsets for H/D atom formation. The action spectrum for forming D atom products is more structured, but in both cases, the structure (though not the yield) disappears once  $\lambda_{\text{phot}} < 265 \text{ nm}$ . These action spectra match well with the previously reported onset of UV absorption and are assigned in terms of excitation to (various vibrational levels of) the  $S_1$  state that dissociates to yield H/D atoms amongst the dissociation products. Torsional structure analogous to that observed in the parent  $C_6H_5SH^+$  two-photon ionization spectrum (Figure 2a) can be expected to accompany each vibrational band in the  $S_1$ – $S_0$  spectrum, which will contribute to the breadths of the individual features in the action spectra for forming H/D atom photoproducts. Given a similar pattern of torsional fine structure to that in Figure 2a, the breadth of the  $S_1$ – $S_0$  origin in  $C_6H_5SH$  (centred at  $\lambda_{\text{phot}} = 285.8 \text{ nm}$ ) can be reproduced by ascribing Lorentzian widths to the individual features, consistent with an excited-state lifetime of  $\sim 130 \text{ fs}$ . This short excited-state lifetime presumably accounts for the non-observation of these broad  $S_1$ – $S_0$  features in the one-color spectrum for forming parent ions.

**3.2. Ab Initio Calculations.** Ab initio calculations using time-dependent density functional theory (TD-DFT) with the HCTH(407) exchange correlation functional<sup>19</sup> were undertaken to ascertain the excited electronic states of  $C_6H_5SH$  that might be important in the wavelength range of interest. The ground-state geometry was optimized at the DFT HCTH/6-311G++(d,p) level. Vertical excitation energies calculated with TD-DFT at this geometry, using the same functional and basis set, are listed in Table 1. These studies confirm that the highest occupied molecular orbital in the ground state is dominated by a nonbonding  $3p\pi$  orbital localized on sulfur and predict that the  $S_1(^1\pi\pi^*)$  state lies at an energy of 4.36 eV, in good agreement with the onsets of both UV absorption (Figure 1) and H atom loss (as revealed by the  $H^+$  action spectrum (Figure 2b)). Two triplet  $\pi^* \leftarrow \pi$  states are predicted at lower excitation energies. The lack of UV absorption at  $\lambda > 294 \text{ nm}$ <sup>17</sup> indicates that these



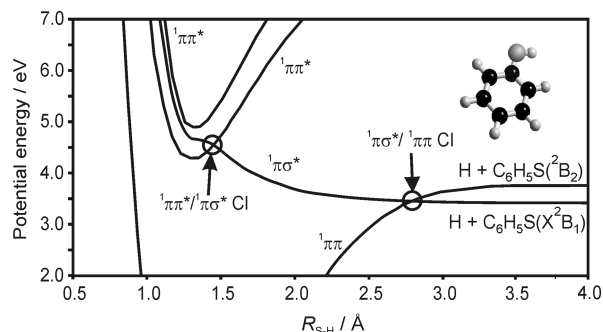


**Figure 3.** Sections, along  $R_{S-H}$ , through the diabatic PESs for the ground,  $1\pi\pi^*$  and  $1\pi\sigma^*$  states of  $C_6H_5SH$ , adapted from Lim et al.<sup>11</sup> to match the energetics derived in the present experiments.

$T_1(^3\pi\pi^*) \leftarrow S_0$  and  $T_2(^3\pi\pi^*) \leftarrow S_0$  excitations have negligible transition moments. However,  $T_n \leftarrow S_0$  absorption near the  $S_1-S_0$  origin could be enhanced by spin-orbit interaction with the  $S_1(^1\pi\pi^*)$  state, and the TD-DFT calculations suggest the  $T_3(^3\pi\sigma^*)$  or, more probably, the  $T_4(^3\pi\pi^*)$  excited state as a possible carrier for the structured parent absorption identified in Figure 2a. The vertical transition to the  $S_2(^1\pi\sigma^*)$  state is predicted at 4.52 eV. The antibonding  $\sigma^*$  orbital is largely localized on the S-H bond, suggesting that this state is likely to be repulsive in the S-H stretch coordinate and identifying this state as the analogue of the  $1\pi\sigma^*$  state implicated in O-H bond fission in phenols.<sup>3-5,12</sup> The  $S_3(^1\pi\pi^*) \leftarrow S_0$  excitation is calculated to lie at  $\sim 4.9$  eV and to have a large oscillator strength, in good accord with the marked increase in parent absorption at  $\lambda \sim 250$  nm<sup>11,17</sup> (see Figure 1).

These findings agree well with the results of higher-level electronic structure calculations reported by Lim et al.<sup>11</sup> These confirm that the ground state of  $C_6H_5SH$  correlates diabatically with the excited  $C_6H_5S(^2B_2)$  state of the radical and that the  $1\pi\sigma^*$  state is indeed dissociative in  $R_{S-H}$ , correlating to ground-state  $C_6H_5S(X^2B_1) + H$  products. As noted previously, these two states of the  $C_6H_5S$  radical differ in the relative orientation of the singly occupied  $3p\pi$  orbital on the sulfur atom which lies, respectively, perpendicular (in the  $X^2B_1$  state) and parallel (in the excited  $^2B_2$  state) to the molecular plane. Thus, the PES of the diabatic  $1\pi\sigma^*$  state must cross those of the diabatic  $1\pi\pi^*$  and ground states, and these crossings must develop into CIs given the appropriate out-of-plane distortion.<sup>3</sup> An approximate potential energy profile, illustrating only the singlet states of thiophenol and based on the ab initio potentials of Lim et al.<sup>11</sup> but scaled to match energetics established in the present experimental study, is displayed in Figure 3. Following the convention set by the early work of Sobolewski et al.<sup>3</sup> and for ease of comparison with the description of our corresponding UV photolysis studies of phenol,<sup>5</sup> we label the CIs of interest in the present work in terms of the interacting diabatic states, that is, the CI at large  $R_{S-H}$  is between the  $1\pi\sigma^*$  and  $1\pi\pi$  diabatic states. The PES of the  $^3\pi\sigma^*$  state was found to lie at a slightly lower vertical excitation energy than its  $1\pi\sigma^*$  analogue and, in the absence of spin-orbit interaction, to correlate with the same asymptotic limit. However, due to spin-orbit interaction, the  $^3\pi\sigma^*$  PES displays an avoided crossing with the (adiabatic) ground-state PES, with the result that the  $^3\pi\sigma^*$  state correlates, asymptotically, with the excited  $C_6H_5S(^2B_2) + H$  radical products. The calculations<sup>11</sup> also reveal a higher-energy dissociative  $^3\sigma\sigma^*$  state, correlating to this same (excited) dissociation limit. At short  $R_{S-H}$ , however, the  $^3\sigma\sigma^*$  state suffers an avoided crossing with the

bound  $T_1(^3\pi\pi^*)$  diabatic state. Thus, the lowest-energy (adiabatic) PES of  $^3A'$  symmetry is calculated to have dominant  $T_1(^3\pi\pi^*)$  character in the vertical Franck-Condon region, repulsive  $^3\sigma\sigma^*$  character at longer  $R_{S-H}$ , and to correlate with the asymptotic products  $C_6H_5S(^2B_2) + H$ .

Guided by these calculations, Lim et al.<sup>11</sup> envisaged three possible fragmentation mechanisms that might account for the anisotropic bimodal velocity distributions observed in their imaging studies of the H/D atoms following 243.1 nm photolysis of  $C_6H_5SH$  and  $C_6H_5SD$ . All assume initial excitation to the repulsive  $1\pi\sigma^*$  PES but differ in the details of the mechanism for subsequent S-H(D) bond rupture. The proposed possibilities involved:

(i) Intersystem crossing (ISC) between the  $1\pi\sigma^*$  and  $^3\pi\sigma^*$  surfaces at short  $R_{S-H}$  before the region of the spin-orbit-induced avoided crossing between the  $^3\pi\sigma^*$  and ground-state PESs, which might allow some  $1\pi\sigma^*$  population to couple onto the  $^3\pi\sigma^*$  PES. Dissociation on the latter surface leads to the excited products  $C_6H_5S(^2B_2) + H$ , whereas dissociation on the  $1\pi\sigma^*$  PES generates ground-state  $C_6H_5S(X^2B_1) + H$  products.

(ii) The CI between the  $1\pi\sigma^*$  surface and the ground state at extended  $R_{S-H}$  could offer a means of coupling flux on the  $1\pi\sigma^*$  PES onto the diabatic  $1\pi\pi$  potential, dissociation on which leads to excited-state products. Flux passing through the CI, however, and remaining on the  $1\pi\sigma^*$  PES would yield ground-state radical products.

(iii) Dissociation on the  $1\pi\sigma^*$  PES to  $C_6H_5S(X^2B_1) + H$  products was envisaged as being in competition with ISC to, and predissociation on, the  $^3\sigma\sigma^*$  surface, which would yield excited-state products.

As shown below, the most straightforward interpretation of the experimental PTS data reported here implies a dominant role for mechanism (ii).

**3.3. H/D Atom Photofragment Translational Energy Spectra.** H/D atom TOF spectra were recorded following photodissociation of  $C_6H_5SH/C_6H_5SD$  at many wavelengths within the range of  $225 \leq \lambda_{\text{phot}} \leq 290$  nm. Consistent with the studies of Lim et al.,<sup>10,11</sup> the fast H/D atoms are deduced to arise via S-H/D bond fission, generating  $C_6H_5S$  radicals as the cofragments. The measured TOF data are converted to total kinetic energy release (TKER) spectra using the relation

$$\text{TKER} = \frac{1}{2} m_{H/D} \left( 1 + \frac{m_{H/D}}{m_R} \right) \left( \frac{d}{t} \right)^2 \quad (1)$$

where  $m_{H/D}$  and  $m_R$  are the mass of the H/D atom ( $m_H = 1.0079$  u/ $m_D = 2.0141$  u) and the partner fragment ( $m_R = 109.17$  u), respectively,  $d$  is the distance separating the interaction volume and the center of the front face of the detector, and  $t$  is the measured H/D atom TOF. Intensity “re-binning” required use of the appropriate  $t^{-3}$  Jacobian for converting such TOF data into TKER space.

Figure 4 shows illustrative H atom TOF spectra recorded following photolysis of  $C_6H_5SH$  at  $\lambda_{\text{phot}} = 290.00$ , 282.80, and 247.50 nm (with  $\epsilon_{\text{phot}}$  aligned at  $\theta = 90^\circ$ ), along with the resulting TKER spectra. The detailed forms of these spectra depend on  $\lambda_{\text{phot}}$ , but all three show two distinct, structured features. These are attributable to formation of  $C_6H_5S$  fragments in various vibrational levels of both the ground ( $X^2B_1$ ) and first excited ( $^2B_2$ ) electronic states. Assignment of this structure relies on DFT (Gaussian 03)<sup>20</sup> calculations (at the B3LYP/6-311g++(d,p) level) of the vibrational wavenumbers of the  $C_6H_5S$  radical in the two electronic states. The results of these calculations, which also

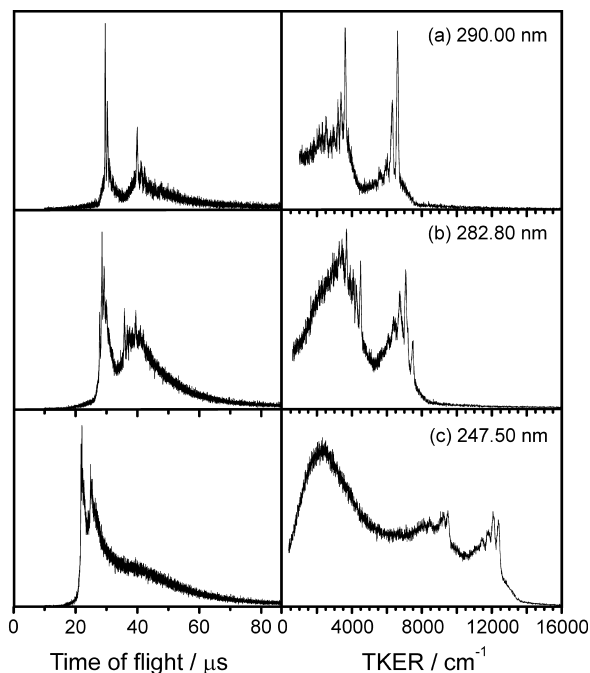


**Figure 4.** H atom TOF spectra and the corresponding TKER spectra of the H + C<sub>6</sub>H<sub>5</sub>S fragments obtained following photolysis of C<sub>6</sub>H<sub>5</sub>SH at  $\lambda_{\text{phot}}$  = (a) 290.00, (b) 282.80, and (c) 247.50 nm, with  $\epsilon_{\text{phot}}$  aligned at  $\theta = 90^\circ$  to the TOF axis.

serve to confirm the planarity of the radical in both electronic states, are listed in Appendix 1. Vibrational wavenumbers for the C<sub>6</sub>H<sub>5</sub>SH parent molecule in its ground state, calculated at the same level of theory, are in good agreement with experimental values,<sup>8</sup> encouraging confidence in the reliability of the predicted radical wavenumbers. The Wilson mode numbering scheme<sup>21</sup> is used throughout since it is insensitive to the loss of the three S–H modes and thus serves to illustrate the complementarity of the ring vibrations in the parent and radical products. The relative peak intensities in the TKER spectra reflect the branching ratios for forming C<sub>6</sub>H<sub>5</sub>S products in specific electronic ( $X^2B_1/2B_2$ ) and vibrational ( $\nu$ ) states, while the widths of the peaks indicates that the radical products are formed with relatively little rotational excitation. As Figure 4c shows, an unstructured feature becomes increasingly evident at low TKER as  $\lambda_{\text{phot}}$  is reduced. The TKER of this broad feature, which is centered at  $\sim 2300$  cm<sup>-1</sup> ( $\sim 3300$  cm<sup>-1</sup> in the case of D atoms from photolysis of C<sub>6</sub>H<sub>5</sub>SD), is largely insensitive to  $\lambda_{\text{phot}}$ . Such observations are very reminiscent of similar broad features observed in the TKER spectra derived from H atom TOF spectra in many other heteroaromatics, for example, phenol,<sup>5</sup> and as in those cases, we attribute this signal to “statistical” unimolecular decay of highly vibrationally excited parent molecules formed by radiationless transfer following one- (and multi-) photon excitation. The detailed forms of the measured TKER spectra evolve with  $\lambda_{\text{phot}}$ . These trends, and their interpretation, are presented below in a number of subsections partitioned to assist the reader.

**3.3.1. Photodissociation at Long Wavelengths,  $\lambda_{\text{phot}} > 275$  nm.** *Overview and  $D_0(\text{C}_6\text{H}_5\text{S}-\text{H})$ .* The action spectra for forming H/D atom products at these wavelengths are structured (Figure 2). As Figure 5 shows, the TKER spectra obtained from H atom TOF spectra recorded in this wavelength range also show the most clearly resolved structure, but polarization studies reveal that the distribution of fragment recoil velocities is isotropic.  $\lambda_{\text{phot}} = 290.00$  nm is the longest wavelength at which H atom

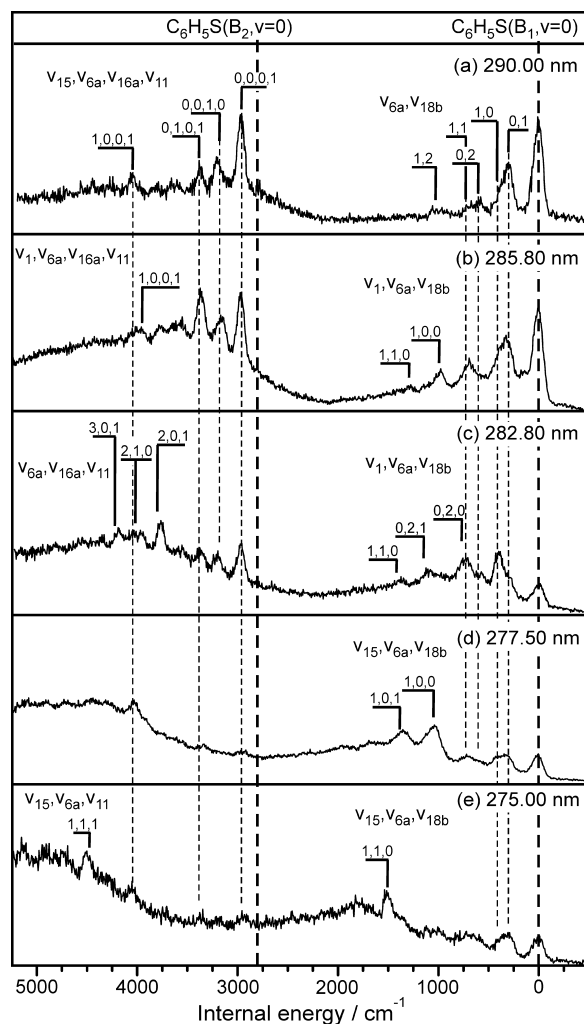


**Figure 5.** Internal energy spectra of C<sub>6</sub>H<sub>5</sub>S radicals formed following excitation of C<sub>6</sub>H<sub>5</sub>SH at  $\lambda_{\text{phot}}$  = (a) 290.00, (b) 285.80, (c) 282.80, (d) 277.50, and (e) 275.00 nm, recorded with  $\epsilon_{\text{phot}}$  aligned at  $\theta = 90^\circ$  to the TOF axis. The assignments have been positioned using the ab initio anharmonic wavenumbers listed in Appendix 1.

formation is observed. Analysis of the TKER spectra obtained at this ((Figure 5a) and neighboring wavelengths allows determination of the S–H bond strength,  $D_0(\text{C}_6\text{H}_5\text{S}-\text{H})$ , via the relationship

$$D_0(\text{C}_6\text{H}_5\text{S}-\text{H}) = E_{\text{phot}} + E_{\text{int}}(\text{C}_6\text{H}_5\text{SH}) - \text{TKER} - E_{\text{int}}(\text{C}_6\text{H}_5\text{S}) \quad (2)$$

where  $E_{\text{int}}(\text{C}_6\text{H}_5\text{SH})$  and  $E_{\text{int}}(\text{C}_6\text{H}_5\text{S})$  are, respectively, the internal energies of the  $S_0$  parent molecule and of the C<sub>6</sub>H<sub>5</sub>S photoproduct. Our analysis of the parent excitation spectrum (Figure 2a) implies a mean value of  $\langle E_{\text{int}}(\text{C}_6\text{H}_5\text{SH}) \rangle \sim 100$  cm<sup>-1</sup>, associated with the appreciable population of torsional levels with  $\tau_{\text{S}-\text{H}} > 0$ . Since the H atoms of interest arise via S–H bond fission, this  $E_{\text{int}}(\text{C}_6\text{H}_5\text{SH})$  cannot be retained in the dissociation; it will be largely converted into TKER, with a small partitioning into framework rotation. The nonzero  $E_{\text{int}}(\text{C}_6\text{H}_5\text{SH})$  thus contributes a  $\sim 100$  cm<sup>-1</sup> shift in the TKER spectra, while the spread of possible  $E_{\text{int}}(\text{C}_6\text{H}_5\text{SH})$  (associated with the photodissociation of parent molecules with  $\tau_{\text{S}-\text{H}} = 0, 1, 2$ , etc.) serves to broaden the observed TKER peaks.

As will be demonstrated below, the peak at the highest TKER in spectra such as that obtained at  $\lambda_{\text{phot}} = 290.00$  nm is most plausibly assigned to formation of H + C<sub>6</sub>H<sub>5</sub>S( $X^2B_1, \nu = 0$ )

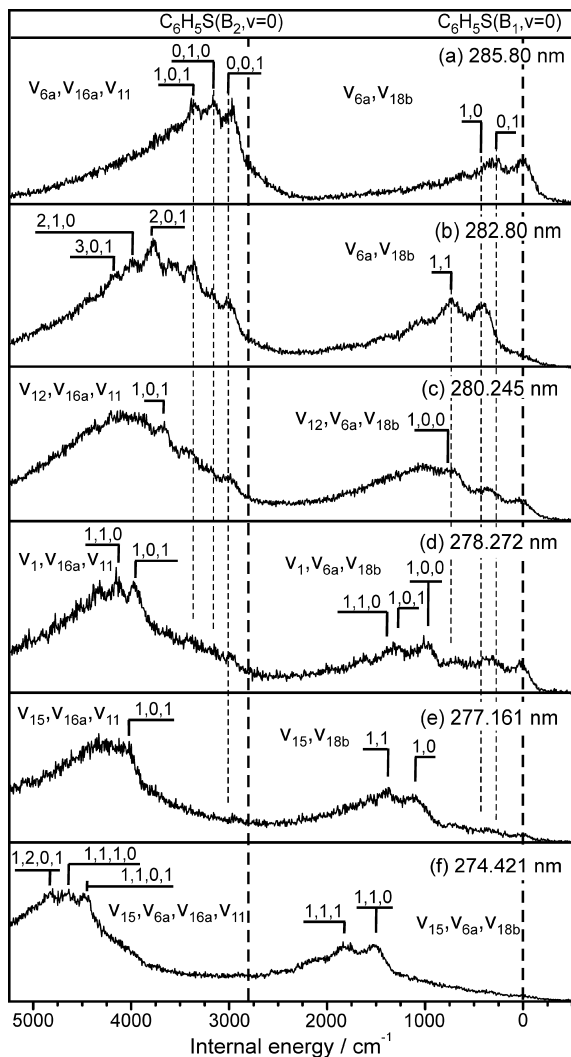


**Figure 6.** Internal energy spectra of  $\text{C}_6\text{H}_5\text{S}$  radicals formed following excitation of  $\text{C}_6\text{H}_5\text{SD}$  at  $\lambda_{\text{phot}} =$  (a) 285.80, (b) 282.80, (c) 280.245, (d) 278.272, (e) 277.161, and (f) 274.421 nm, recorded with  $\epsilon_{\text{phot}}$  aligned at  $\theta = 90^\circ$  to the TOF axis. The assignments have been positioned using the ab initio anharmonic wavenumbers listed in Appendix 1.

products (i.e., products with  $E_{\text{int}}(\text{C}_6\text{H}_5\text{S}) = 0$ ). Given this assignment, and assuming  $\langle E_{\text{int}}(\text{C}_6\text{H}_5\text{SH}) \rangle = 100 \text{ cm}^{-1}$ , eq 2 yields  $D_0(\text{C}_6\text{H}_5\text{S}-\text{H}) = 28030 \pm 100 \text{ cm}^{-1}$  ( $335.3 \pm 1.2 \text{ kJ mol}^{-1}$ ). As discussed below, this value should be regarded as an upper limit since we cannot definitively exclude the possibility that all of the products carry an additional (unrecognized) quantum of vibration. A similar analysis of the (less well resolved) TKER spectra of  $\text{D} + \text{C}_6\text{H}_5\text{S}$  products resulting from long-wavelength photolysis of  $\text{C}_6\text{H}_5\text{SD}$ , again assuming  $E_{\text{int}}(\text{C}_6\text{H}_5\text{SD}) = 100 \text{ cm}^{-1}$  as a result of the population of excited torsional levels of the  $\text{S}_0$  state, yields  $D_0(\text{C}_6\text{H}_5\text{S}-\text{D}) \leq 28610 \pm 100 \text{ cm}^{-1}$ . The difference between  $D_0(\text{C}_6\text{H}_5\text{S}-\text{D})$  and  $D_0(\text{C}_6\text{H}_5\text{S}-\text{H})$ ,  $\sim 580 \text{ cm}^{-1}$ , agrees sensibly with the difference in the zero-point energies of the three modes that disappear upon  $\text{S}-\text{H}(\text{D})$  bond fission. The bond dissociation energy determined here is in reasonable agreement with (and defined to higher precision than) the previous experimental estimates of this quantity<sup>11,22–24</sup> and with the reported theoretical values.<sup>11,24–29</sup>

Given  $D_0(\text{C}_6\text{H}_5\text{S}-\text{H})$ , eq 2 can be rearranged so that TKER spectra can be replotted on a common  $E_{\text{int}}(\text{C}_6\text{H}_5\text{S})$  internal energy scale, which is independent of  $\lambda_{\text{phot}}$  and aids assignment of the vibrational energy disposal within these products. The spectra displayed in Figure 5 are plotted in this way, as are the

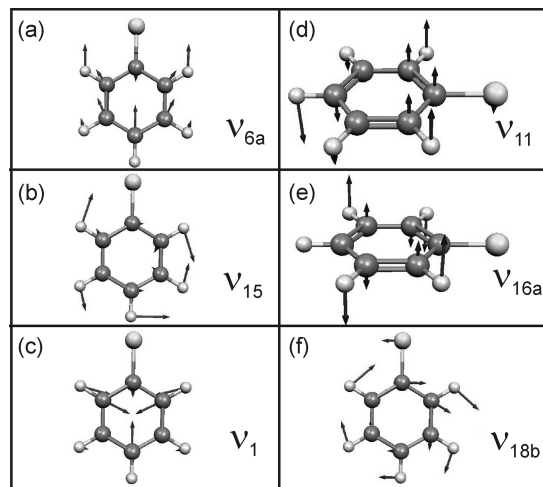


**Figure 7.** Illustrations of the nuclear motions associated with active vibrational modes identified in the  $\text{C}_6\text{H}_5\text{S}$  products arising in the long-wavelength photolysis of  $\text{C}_6\text{H}_5\text{SH}$  and  $\text{C}_6\text{H}_5\text{SD}$ ; (a–c) show the in-plane vibrations induced by dynamic (dFC) or vertical (vFC) Franck–Condon effects, (d) and (e) show the modes induced by dynamics at the conical intersection, and (f) shows the C–S wagging vibration,  $\nu_{18b}$ , induced impulsively during the dissociation.

corresponding spectra obtained by monitoring D atom loss following excitation of  $\text{C}_6\text{H}_5\text{SD}$  in this same long-wavelength range (Figure 6). Peak assignments, based on the calculated vibrational wavenumbers listed in Appendix 1, are shown above the relevant spectra in these figures. Each spectrum shows a number of characteristic features, which are now reviewed.

**Energy Disposal and Product Mode Assignments.** Consider the  $\lambda_{\text{phot}} = 290.00 \text{ nm}$  data shown in Figure 5a. The peak separations in the low  $E_{\text{int}}(\text{C}_6\text{H}_5\text{S})$  region are noticeably wider than those at higher internal energy. The former structure can be assigned in terms of formation of ground-state  $\text{C}_6\text{H}_5\text{S}(\text{X}^2\text{B}_1)$  radicals in their  $v = 0$  level and in levels carrying one or two quanta of excitation in modes  $\nu_{18b}$  (the in-plane C–S wag) and  $\nu_{6a}$  (a symmetric ring breathing mode). For future reference, the nuclear motions associated with these and other modes, introduced subsequently, are displayed in Figure 7. The set of peaks beginning at  $E_{\text{int}}(\text{C}_6\text{H}_5\text{S}) = 2960 \text{ cm}^{-1}$  is assigned to the  $\text{C}_6\text{H}_5\text{S}(\text{X}^2\text{B}_2) + \text{H}$  product channel. However, the spacings between these peaks cannot be assigned using the vibrational wavenumbers listed in Appendix 1 if the  $2960 \text{ cm}^{-1}$  peak is assigned to  $\text{C}_6\text{H}_5\text{S}(\text{X}^2\text{B}_2, v = 0)$  products. These, and the companion peaks in all spectra displayed in Figures 5 and 6, can only be assigned consistently if the  $2960 \text{ cm}^{-1}$  feature is associated with formation of  $\text{C}_6\text{H}_5\text{S}(\text{X}^2\text{B}_2)$  radicals with one quantum of excitation in the lowest-frequency  $a''$  mode ( $\nu_{11}$ , a ring-puckering vibration with  $b_1(C_{2v})$  symmetry). The peak at  $E_{\text{int}}(\text{C}_6\text{H}_5\text{S}) = 3215 \text{ cm}^{-1}$  can then be assigned to  $\text{C}_6\text{H}_5\text{S}(\text{X}^2\text{B}_2)$  products carrying a quantum of  $\nu_{16a}$  (another low-frequency  $a''$  ring-puckering mode of  $a_2$  symmetry in  $C_{2v}$ ). The peaks at  $E_{\text{int}}(\text{C}_6\text{H}_5\text{S}) = 3420$  and at  $\sim 4090 \text{ cm}^{-1}$  are consistent with formation of  $\text{C}_6\text{H}_5\text{S}(\text{X}^2\text{B}_2)$  radicals carrying one quantum of  $\nu_{11}$  together with, respectively, a quantum of  $\nu_{6a}$  or  $\nu_{15}$  (both of which are in-plane ring breathing modes). Significantly, these assignments imply that all modes active in the  $\text{C}_6\text{H}_5\text{S}(\text{X}^2\text{B}_1)$  products have  $a'$  vibrational symmetry, whereas the populated levels of the  $\text{C}_6\text{H}_5\text{S}(\text{X}^2\text{B}_2)$  products all have  $a''$  vibrational symmetry. Given these assignments, the energy difference between the electronic origins of the  $\text{X}^2\text{B}_1$  and  $\text{X}^2\text{B}_2$  states of the thiophenoxyl radical is determined as  $T_{00} = 2800 \pm 40 \text{ cm}^{-1}$ , in reasonable accord with a recent theoretical estimate ( $2674 \text{ cm}^{-1}$  (ref 11)).



The spectrum obtained at  $\lambda_{\text{phot}} = 285.80$  nm (Figure 5b) is very similar, though the branching into levels carrying a quantum of  $\nu_{6a}$  is enhanced in both product channels and additional peaks appear that are attributable to the population of levels carrying a quantum of  $\nu_1$  (another symmetric ring breathing mode; see Figure 7). The  $\lambda_{\text{phot}} = 282.80$  nm spectrum (Figure 5c), obtained following excitation at the maximum of the second peak in the action spectrum for forming H atom products (Figure 2b), again shows some similarities but also noteworthy differences. The relative yield of  $\text{C}_6\text{H}_5\text{S}(\text{X}^2\text{B}_1, \nu = 0)$  radicals is much reduced, but new features attributable to the population of levels with  $\nu_{16a} \geq 2$  appear (particularly in the  $\text{C}_6\text{H}_5\text{S}(\text{S}^2\text{B}_2)$  product channel), suggesting that  $\nu_{6a}$  may be active in the  $\text{S}_1 \leftarrow \text{S}_0$  excitation at this wavelength. Similar behavior (albeit involving different in-plane modes) is observed at  $\lambda_{\text{phot}} = 277.50$  and  $275.00$  nm, resonant with further weak peaks in the action spectrum for forming H atom products. The strongest features in the former spectrum (Figure 5d) indicate population of levels involving  $\nu_{15} = 1$  (alone in the case of the  $\text{X}^2\text{B}_1$  products and in combination with  $\nu_{11} = 1$  in the case of  $\text{C}_6\text{H}_5\text{S}(\text{S}^2\text{B}_2)$ ), whereas peaks attributable to population of combination levels with excitation in both  $\nu_{15}$  and  $\nu_{6a}$  are clearly evident in the  $\lambda_{\text{phot}} = 275.00$  nm spectrum (Figure 5e).

As Figure 6 shows, similar trends are found in the  $E_{\text{int}}(\text{C}_6\text{H}_5\text{S})$  spectra obtained following long-wavelength photolysis of  $\text{C}_6\text{H}_5\text{SD}$ . The data obtained at  $\lambda_{\text{phot}} = 285.80$  and  $282.80$  nm (Figure 6a and b), following excitation at the centers of the first two broad features in the action spectrum for forming D atoms (Figure 2c) reveal  $E_{\text{int}}(\text{C}_6\text{H}_5\text{S})$  distributions similar to, though less well resolved than, those seen in the analogous  $\text{C}_6\text{H}_5\text{SH}$  studies (Figure 5b and c). As in that case, the structure is interpretable in terms of the population of levels involving  $\nu_{6a}$  and  $\nu_{18b}$  (in combination with the out-of-plane mode  $\nu_{11}$  in the case of the  $\text{S}^2\text{B}_2$  products). The poorer resolution of these TKER spectra is most probably a reflection of increased rotational excitation of the  $\text{C}_6\text{H}_5\text{S}$  product as a result of the greater impulse accompanying S–D bond fission. Similar trends have been noted when comparing peak shapes in TKER spectra of the H + pyrrolyl and D + pyrrolyl- $d_4$  products resulting from UV photolysis of pyrrole and pyrrole- $d_5$ .<sup>13,30</sup> Moving to shorter  $\lambda_{\text{phot}}$ , weak features indicative of population in product modes involving quanta of  $\nu_{12}$  (at  $\lambda_{\text{phot}} = 280.245$  nm, Figure 6c),  $\nu_1$  (at  $\lambda_{\text{phot}} = 278.272$  nm, Figure 6d),  $\nu_{15}$  (at  $\lambda_{\text{phot}} = 277.161$  nm, Figure 6e), and the combination mode  $\nu_{15} + \nu_{6a}$  (at  $\lambda_{\text{phot}} = 274.421$  nm, Figure 6f) are recognizable as is the general trend for the population distribution within both product channels to shift to higher internal energy.

Several of the foregoing observations have clear parallels with previous findings regarding the photofragmentation of phenol following excitation near its  $\text{S}_1\text{--S}_0$  origin.<sup>5</sup> The finding that the H(D) atoms formed at these long wavelengths have isotropic recoil velocity distributions suggests that the dissociation time scale is longer than the rotational period of the excited-state molecule. Such an observation is consistent with the assumption that the initial absorption is to the  $^1\pi\pi^*$  ( $\text{S}_1$ ) state. Reference to Figure 3 suggests that subsequent S–H(D) bond fission must involve radiationless transfer to the  $^1\pi\sigma^*$  PES, either directly by tunnelling from  $\text{S}_1$  or possibly, as in the case of phenol, via internal conversion to high vibrational levels of the  $^1\pi\pi$  state and subsequent transfer at the long-range CI between the diabatic  $^1\pi\sigma^*$  and  $^1\pi\pi$  PESs. The foregoing product vibrational state assignments provide further insights into the dissociation dynamics.

**Symmetry Considerations.** The  $\text{S}_1$  (and  $\text{S}_0$ ) states of the parent molecule have  $\text{A}'$  electronic symmetry, whereas the  $^1\pi\sigma^*$  state has  $\text{A}''$  electronic symmetry. The  $\text{X}^2\text{B}_1$  state of the  $\text{C}_6\text{H}_5\text{S}$  radical transforms as  $\text{A}''$  in the  $\text{C}_s$  point group of the parent, while the  $^2\text{B}_2$  excited state of the radical has  $\text{A}'$  symmetry. Experimentally, we observe population of  $\text{a}'$  vibrational levels of the  $\text{X}^2\text{B}_1$  state product and  $\text{a}''$  vibrational levels of the  $^2\text{B}_2$  state radical, that is, all identified product levels have  $\text{A}''$  vibronic symmetry. Consider parent excitation at the  $\text{S}_1\text{--S}_0$  origin. Both  $\nu = 0$  levels have  $\text{a}'$  vibrational (and  $\text{A}'$  vibronic) symmetry. Indeed, Franck–Condon arguments require that *any*  $\text{S}_1$  level populated by excitation from the  $\text{S}_0(\nu = 0)$  level should have  $\text{A}'$  vibronic symmetry. (As noted previously, a significant fraction of the  $\text{C}_6\text{H}_5\text{SH}(\text{C}_6\text{H}_5\text{SD})$  sample in the present experiments is in levels with  $\tau_{\text{S–H}} = \text{odd}$ ; therefore, the ensemble of photoexcited molecules is likely to contain states of both  $\text{A}'$  and  $\text{A}''$  vibronic symmetry.) Overall vibronic symmetry must be conserved in the subsequent evolution to dissociation products. On this basis, products with  $\text{A}'$  vibronic symmetry might have been expected, contrary to observation. This apparent dichotomy can be resolved, however, if we assume that coupling between the diabatic  $^1\pi\pi^*$  and  $^1\pi\sigma^*$  PESs is mediated by S–H torsion (an  $\text{a}''$  mode). Transfer of flux from an  $^1\pi\pi^*$  level of  $\text{A}'(\text{A}'')$  vibronic symmetry would thus result in population of  $^1\pi\sigma^*$  levels carrying an odd(even) number of quanta in  $\tau_{\text{S–H}}$ . Motion in this mode must “soften” upon S–H extension, however, and eventually be lost as product translation (and/or framework rotation). As mentioned previously, we recognize the possibility that all of the observed product states might carry an additional quantum of vibration in another  $\text{a}''$  mode arising as a result of the  $^1\pi\pi^*/^1\pi\sigma^*$  coupling, as observed in the case of phenol photolysis at  $\lambda_{\text{phot}} < 246$  nm, where all phenoxyl fragments are deduced to carry a quantum of  $\nu_{16b}$ .<sup>5</sup> Unfortunately, these two possibilities are not distinguishable in the present experiments; the consequence of the alternative interpretation (and the resulting offset of the implied  $E_{\text{int}}$ ) would be to lower the bond strength estimates given above.

**Mode-Specific, Nonadiabatic Dissociation Dynamics.** The deduced energy disposal shows a number of interesting contrasts with that observed in the case of phenol following photoexcitation to low vibrational levels of its  $\text{S}_1(^1\pi\pi^*)$  state. This first concerns the mechanism by which flux transfers to the  $^1\pi\sigma^*$  state, which, in the case of thiophenol, even at the longest excitation wavelengths, is deduced to involve (S–H torsion induced) coupling at the  $^1\pi\pi^*/^1\pi\sigma^*$  CI. In contrast to the phenol case, there is no “shift” in the deduced  $E_{\text{int}}$  of the peak at highest TKER upon varying  $\lambda_{\text{phot}}$ , implying a common fragmentation mechanism (i.e., via the  $^1\pi\pi^*/^1\pi\sigma^*$  CI) across the wavelength range investigated. The evolving flux is therefore sensitive to the upper part of the CI between the diabatic  $^1\pi\sigma^*$  and  $^1\pi\pi$  PESs at longer  $R_{\text{S–H}}$ , in contrast to the case of phenol at long  $\lambda_{\text{phot}}$ , where the dissociating molecules are deduced to sample the lower part of the corresponding CI after internal conversion to high vibrational levels of the ground state.<sup>5</sup> A second difference arises at the  $^1\pi\sigma^*/^1\pi\pi$  CI itself, where, in the case of the  $\text{C}_6\text{H}_5\text{SH}$ , dissociating flux has the opportunity to branch into two different electronic states of the  $\text{C}_6\text{H}_5\text{S}$  product. The corresponding first excited  $^2\text{B}_2$  state in the phenoxyl radical lies  $\sim 8900$   $\text{cm}^{-1}$  above the ground state,<sup>31</sup> reflecting the much greater interaction between the singly occupied  $p\pi$  orbital of the heteroatom and the  $\pi$  system of the ring in the case of  $\text{C}_6\text{H}_5\text{O}$ . As a result, the  $^1\pi\sigma^*/^1\pi\pi$  CI in phenol occurs at shorter  $R_{\text{X–H}}$  bond lengths, the difference in the respective potential gradients in the region of the intersection is much greater,

**TABLE 2: Wavelengths and Wavenumbers of Prominent Peaks in the Action Spectrum for Forming D Atoms Following Photolysis of C<sub>6</sub>H<sub>5</sub>SD Molecules, Together with Vibronic Assignments Proposed by Analysis of the Accompanying TKER Spectra and the Approximate Vibrational Term Values (relative to the S<sub>1</sub> origin)**

$\lambda_{\text{phot}} / \text{nm}$	$\tilde{\nu}_{\text{phot}} / \text{cm}^{-1}$	S <sub>1</sub> –S <sub>0</sub> transition	S <sub>1</sub> term value / cm <sup>−1</sup>
285.80	34990	0 <sub>0</sub> <sup>0</sup>	0
282.80	35360	6a <sub>0</sub> <sup>1</sup>	370
280.25	35680	12 <sub>0</sub> <sup>1</sup>	690
278.27	35940	1 <sub>0</sub> <sup>1</sup>	950
277.16	36080	15 <sub>0</sub> <sup>1</sup>	1090
275.31	36320	1 <sub>0</sub> <sup>1</sup> + 6a <sub>0</sub> <sup>1</sup>	1330
274.42	36440	15 <sub>0</sub> <sup>1</sup> + 6a <sub>0</sub> <sup>1</sup>	1450

dissociating flux shows a greater tendency to follow the diabatic pathway, and dissociation to electronically excited phenoxyl products is excluded on energetic grounds (except at much shorter  $\lambda_{\text{phot}}$ , or following prior excitation to selected vibrational levels within the ground state.<sup>32</sup>)

The product energy disposal can thus be rationalized as follows. Flux on the <sup>1</sup> $\pi\sigma^*/{}^1\pi\pi$  PES that follows the diabatic route through the <sup>1</sup> $\pi\sigma^*/{}^1\pi\pi$  CI evolves to H + C<sub>6</sub>H<sub>5</sub>S(X<sup>2</sup>B<sub>1</sub>) products. Vibronic symmetry conservation requires that these products are formed in a' vibrational levels, as observed. Dissociation following excitation to the S<sub>1</sub> origin level results in population of product modes  $\nu_{18b}$  and  $\nu_{6a}$ , as well as the  $\nu = 0$  level. Activity in the former mode is understandable in terms of the (relatively weak, in-plane) impulse exerted by the departing H(D) atom, while the observed activity in  $\nu_{6a}$  likely reflects changes in this low-frequency ring vibration during the evolution from the excited parent molecule to product radical. Such excitations will be described as dynamic Franck–Condon (dFC) effects from hereon. As in phenol,<sup>5</sup> activity in other a' vibrational modes ( $\nu_1$ ,  $\nu_{6a}$ ,  $\nu_{12}$ ,  $\nu_{15}$ , and the  $\nu_{6a} + \nu_{15}$  combination mode in the case of thiophenol) identified when exciting at selected shorter wavelengths in this range can be explained in terms of conservation of “spectator” modes that are introduced in the S<sub>1</sub> ← S<sub>0</sub> excitation step and carry through, adiabatically, into the products. Such product excitations will henceforth be described as originating from vertical Franck–Condon (vFC) excitation within the parent. Given the close similarities in the wavenumbers of each of these conserved modes in the (ground-state) parent and the corresponding modes in both states of the radical (see Appendix 1), identifying these modes offers a route to assigning the diffuse structure within the respective action spectra for forming H and D atoms. Assignments derived in this way for some of the more intense features in the action spectrum for forming D atoms from photolysis of C<sub>6</sub>H<sub>5</sub>SD (Figure 2c) are collected in Table 2. We note that the first three such separations match very well with those identified in the earlier analysis of the structured parent REMPI spectrum, implying that, at least with regards to these in-plane ring motions, the geometry of, and bonding within, the excited state providing the resonance enhancement is very similar to that in the <sup>1</sup> $\pi\pi^*(S_1)$  state.

Flux on the <sup>1</sup> $\pi\sigma^*$  PES that follows the adiabatic route through the <sup>1</sup> $\pi\sigma^*/{}^1\pi\pi$  CI evolves to C<sub>6</sub>H<sub>5</sub>S(<sup>2</sup>B<sub>2</sub>) excited-state products. Vibronic symmetry conservation in this case requires that these products are formed in a'' vibrational levels, again as observed. The most obvious features in this product channel when exciting via the S<sub>1</sub> origin indicate population of levels with  $\nu_{11} = 1$  or  $\nu_{16a} = 1$ ; no  $\nu = 0$  products are observed. Interestingly, the recent PTS studies of phenol dissociation via the corresponding <sup>1</sup> $\pi\sigma^*/{}^1\pi\pi$  CI identified activity in these same two coupling

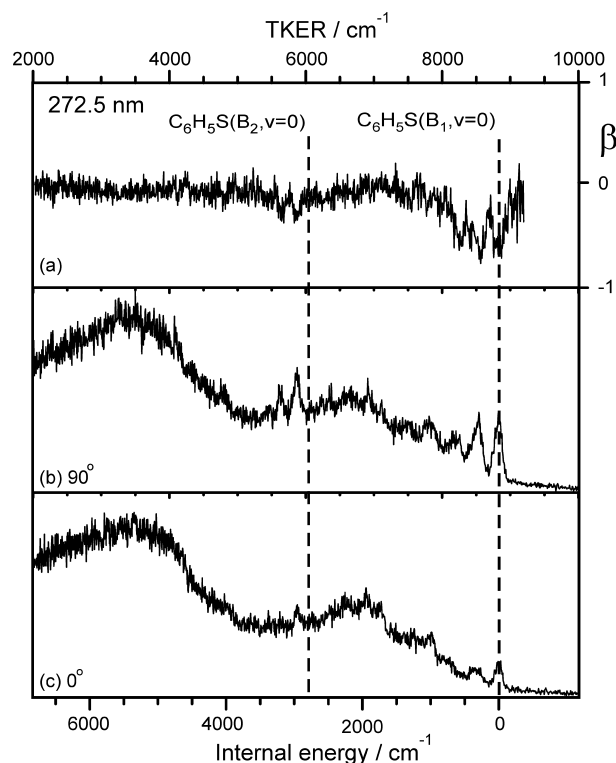


**Figure 8.** Internal energy spectra of C<sub>6</sub>H<sub>5</sub>S radicals formed following excitation of C<sub>6</sub>H<sub>5</sub>SH at  $\lambda_{\text{phot}} = 272.50$  nm, recorded with  $\epsilon_{\text{phot}}$  aligned at  $\theta = 90^\circ$  (b) and  $0^\circ$  (c) to the TOF axis; (a) shows the deduced variation of  $\beta$  with  $E_{\text{int}}(\text{C}_6\text{H}_5\text{S})$  and thus TKER.

modes.<sup>5</sup> As in that case, the implication of this vibrational assignment is that parent modes  $\nu_{11}$  and  $\nu_{16a}$  can both be activated by coupling at the <sup>1</sup> $\pi\sigma^*/{}^1\pi\pi$  CI, with the former seemingly the more active coupling mode in this case. These, and  $\tau_{\text{S-H}}$ , will henceforth be referred to as CI-induced coupling modes. Population of other levels, involving a' modes in combination with  $\nu_{11}$  or  $\nu_{16a}$ , is identifiable in spectra recorded at shorter  $\lambda_{\text{phot}}$ . The active a' modes are largely the same as the dFC and vFC modes identified in the X<sup>2</sup>B<sub>1</sub> radical products, but again, some subtle differences can be recognized. For example, the spectrum recorded at  $\lambda_{\text{phot}} = 290$  nm reveals activity in  $\nu_{18b}$  (the in-plane C–S bend, which we have identified as a dFC mode) in the ground-state products but not in the <sup>2</sup>B<sub>2</sub> product channel. Is this simply a consequence of the reduced TKER associated with these excited state products (and thus the reduced impulse from the departing H/D atom), or does it hint that fragmentation to excited-state products is favored by nonplanar or more collinear dissociation geometries?

**3.3.2. Photodissociation at Wavelengths  $\lambda_{\text{phot}} < 275$  nm.** *Product-Mode Assignments and Recoil Anisotropy.* The  $E_{\text{int}}(\text{C}_6\text{H}_5\text{S})$  spectrum obtained following excitation of C<sub>6</sub>H<sub>5</sub>SH at  $\lambda_{\text{phot}} = 275.00$  nm (Figure 5e) hides a subtlety; this is the longest-wavelength spectrum within which the faster features exhibit discernible recoil anisotropy. Recoil anisotropy can be seen more clearly in data recorded at shorter wavelengths, for both C<sub>6</sub>H<sub>5</sub>SH and C<sub>6</sub>H<sub>5</sub>SD. By way of illustration, Figure 8 shows  $E_{\text{int}}(\text{C}_6\text{H}_5\text{S})$  spectra from C<sub>6</sub>H<sub>5</sub>SH photolysis at  $\lambda_{\text{phot}} = 272.50$  nm recorded with  $\epsilon_{\text{phot}}$  aligned at, respectively,  $\theta = 0^\circ$  (c) and  $90^\circ$  (b) to the TOF axis. The structure evident in Figure 8b is reminiscent of that seen at the longest  $\lambda_{\text{phot}}$  (Figure 5a) and can be assigned accordingly, but these spectra also reveal more population of levels with higher internal energy, in both product channels. These data, together with the corresponding spectra recorded with  $\epsilon_{\text{phot}}$  aligned at  $\theta = 54.7^\circ$ , allow self-



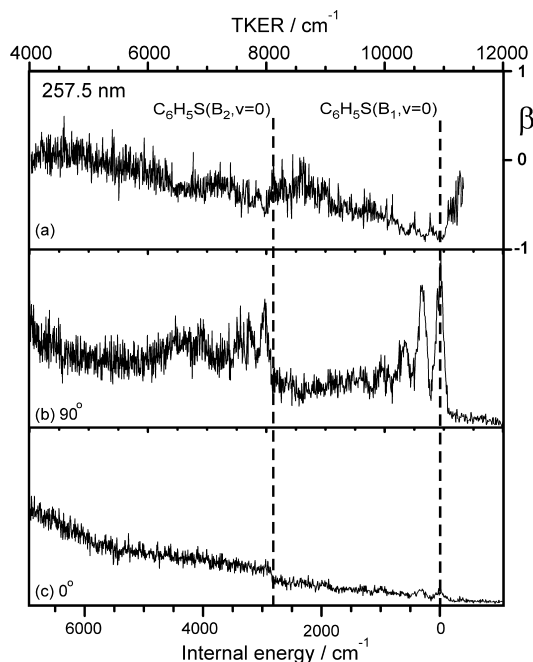


**Figure 9.** Internal energy spectra of  $\text{C}_6\text{H}_5\text{S}$  radicals formed following excitation of  $\text{C}_6\text{H}_5\text{SH}$  at  $\lambda_{\text{phot}} = 257.50$  nm, recorded with  $\epsilon_{\text{phot}}$  aligned at  $\theta = 90^\circ$  (b) and  $0^\circ$  (c) to the TOF axis; (a) shows the deduced variation of  $\beta$  with  $E_{\text{int}}(\text{C}_6\text{H}_5\text{S})$  and thus TKER.

normalization of the respective spectra and determination of the TKER (and  $E_{\text{int}}(\text{C}_6\text{H}_5\text{S})$ ) dependence of the recoil anisotropy parameter,  $\beta$  (Figure 8a).<sup>15</sup> Three features of these data merit particular note. First, branching into the lowest energy levels of the excited  $\text{C}_6\text{H}_5\text{S}(^2\text{B}_2)$  products at  $\lambda_{\text{phot}} = 272.50$  nm is noticeably stronger than that at  $\lambda_{\text{phot}} = 275.00$  or  $277.50$  nm (Figure 5e and d). Second, the fastest features in both product channels are more prominent in the spectra recorded with  $\epsilon_{\text{phot}}$  perpendicular to the detection axis; the fastest features display a recoil anisotropy characterized by  $\beta \sim -0.45$ , whereas the unresolved signal appears essentially isotropic. [The apparent  $|\beta|$  associated with the fastest  $\text{H} + \text{C}_6\text{H}_5\text{S}(^2\text{B}_2)$  products in Figure 8a is reduced by the larger isotropic contribution from  $\text{H} + \text{C}_6\text{H}_5\text{S}(\text{X}^2\text{B}_1, \nu)$  products appearing at the same TKER]. Third, the population distribution in both product channels spreads to higher  $E_{\text{int}}(\text{C}_6\text{H}_5\text{S})$  as  $\lambda_{\text{phot}}$  is reduced, with the result that the “dip” separating the product channels in TKER spectra recorded at long  $\lambda_{\text{phot}}$  (see, e.g., Figure 5) gradually fills.

The transition dipole moment for  $\text{S}_1 \leftarrow \text{S}_0(\pi^* \leftarrow \pi)$  excitation lies in the plane of the molecule and roughly parallel to the S–H bond, whereas the transition dipole associated with excitation to the  $^1\pi\sigma^*(\text{S}_2)$  state lies normal to the plane of the benzene ring and thus also perpendicular to the S–H bond (at the planar equilibrium geometry). The isotropy of the recoiling products observed at  $\lambda_{\text{phot}} > 275$  nm has been rationalized in terms of  $\text{S}_1 \leftarrow \text{S}_0$  excitation, relatively slow transfer (by tunnelling) to the  $^1\pi\sigma^*$  PES, and subsequent dissociation via the  $^1\pi\sigma^*/^1\pi\pi$  CI at longer  $R_{\text{S-H}}$ . Once  $\lambda_{\text{phot}} < 275$  nm, the  $\text{C}_6\text{H}_5\text{S}$  fragments with the lowest internal energies in each product channel display perpendicular recoil anisotropy, whereas the more internally excited products continue to exhibit isotropic velocity distributions. Such behavior can be rationalized by assuming that excitation at  $\lambda_{\text{phot}} < 275$  nm populates both the  $^1\pi\pi^*(\text{S}_1)$  and  $^1\pi\sigma^*(\text{S}_2)$  excited states directly. Extrapolating the trends observed at longer  $\lambda_{\text{phot}}$  suggests that vFC modes excited by  $\text{S}_1 \leftarrow \text{S}_0$  excitation at these wavelengths will map into the corresponding vibrational motions in the  $\text{C}_6\text{H}_5\text{S}$  fragments.

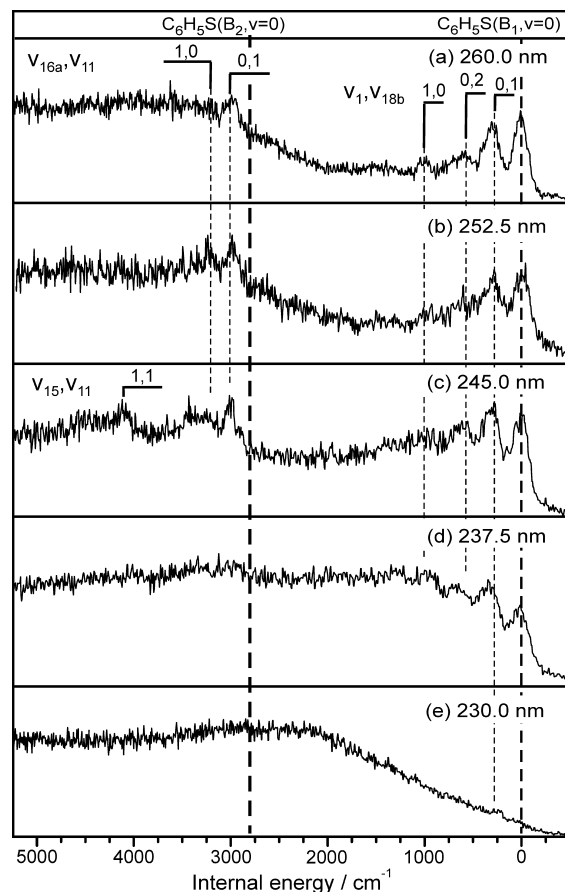


**Figure 10.** TKER spectra derived from H atom TOF spectra (with the assumption that all cofragments have the mass of  $\text{C}_6\text{H}_5\text{S}$ ) measured following photolysis of  $\text{C}_6\text{H}_5\text{SH}$  at  $\lambda_{\text{phot}} =$  (a) 260.00, (b) 252.50, (c) 245.00, (d) 237.50, and (e) 230.00 nm, with  $\epsilon_{\text{phot}}$  aligned at  $\theta = 90^\circ$  to the TOF axis. The maximum possible TKER associated with one-photon production of  $\text{C}_6\text{H}_5\text{S}(\text{X}^2\text{B}_1)$  and  $\text{C}_6\text{H}_5\text{S}(^2\text{B}_2)$  fragments is indicated in each case.

Excitation in spectator modes will provide negligible enhancement to the  $^1\pi\pi^*(\text{S}_1)$  to  $^1\pi\sigma^*$  tunnelling probability, and given the time scales involved, the internally excited products that result would be expected to show little recoil anisotropy, as observed. The  $\text{S}_2 \leftarrow \text{S}_0(\sigma^* \leftarrow \pi)$  excitation, in contrast, populates an excited state that dissociates directly. Symmetry requires that the resulting products should show perpendicular recoil anisotropy (i.e.,  $\beta < 0$ ), again as observed. The vibrational energy disposal accompanying direct dissociation on the  $^1\pi\sigma^*$  PES is found to mimic that observed at  $\lambda_{\text{phot}} = 290$  nm, where the same  $^1\pi\sigma^*$  PES is deduced to be accessed by tunneling of  $\text{S}_1$  molecules prepared with no internal excitation, supporting the view that this product branching is determined largely by the  $^1\pi\sigma^*/^1\pi\pi$  CI.

Many of the trends noted when comparing the  $\lambda_{\text{phot}} = 272.50$  nm data with that obtained at longer wavelength become increasingly evident as  $\lambda_{\text{phot}}$  is reduced further. As Figure 9 shows, the fastest features in both product channels formed at  $\lambda_{\text{phot}} = 257.50$  nm exhibit perpendicular anisotropy ( $\beta \sim -0.85$  for the fastest  $\text{H} + \text{C}_6\text{H}_5\text{S}(\text{X}^2\text{B}_1)$  products), whereas again, the unresolved signal appears more isotropic. A similar preference for perpendicular recoil was also identified in the recent ion imaging studies of H(D) atom photoproducts from  $\text{C}_6\text{H}_5\text{SH}(\text{C}_6\text{H}_5\text{SD})$  photolysis at  $\lambda_{\text{phot}} = 243.1$  nm.<sup>10,11</sup> Figure 10 shows TKER spectra obtained when exciting with  $\epsilon_{\text{phot}}$  aligned perpendicular to the TOF axis at several well-separated wavelengths in the range of  $230.0 \leq \lambda_{\text{phot}} \leq 260.0$  nm. Short

progressions attributable to formation of  $\text{C}_6\text{H}_5\text{S}(\text{X}^2\text{B}_1)$  products with  $\nu_{18b} \leq 3$  are evident in all but the  $\lambda_{\text{phot}} = 230.0$  nm spectrum, as is a peak associated with  $\text{C}_6\text{H}_5\text{S}(\text{X}^2\text{B}_2, \nu_{11} = 1)$  fragments. The excited-state product channel is particularly evident in the  $\lambda_{\text{phot}} = 245$  nm spectrum (i.e., at photolysis wavelengths close to that investigated by Lim et al.<sup>10,11</sup>), and additional structure attributable to the population of levels involving activity in  $\nu_{15}$  as well as  $\nu_{11}$  is apparent. The family of spectra shown in Figure 10 provides further illustration of the progressive coalescence of the TKER distributions associated with the  $\text{C}_6\text{H}_5\text{S}(\text{X}^2\text{B}_1)$  and  $\text{C}_6\text{H}_5\text{S}(\text{X}^2\text{B}_2)$  product channels and of the substantial contribution from the broad feature centered at low TKER that we attribute to “statistical” decay of highly internally excited parent molecules (recall Figure 4c), both of which lead to a progressive loss of structure in TKER spectra recorded at shorter  $\lambda_{\text{phot}}$ .

Recalling the parent absorption spectrum (Figure 1) and the calculated vertical excitation energies (Table 1), it is evident that the dominant excitation at  $\lambda_{\text{phot}} \leq 260$  nm is likely to be to the  $\text{S}_3(^1\pi\pi^*)$  state. The present TD-DFT calculations show the  $\text{S}_3 \leftarrow \text{S}_0$  transition moment lying in the plane of the molecule but at  $\sim 90^\circ$  to the S–H bond. Discussion of the fragmentation mechanism at these shorter wavelengths must, of necessity, be speculative, given our ignorance of the one or more CIs that facilitate population transfer from the photoprepared  $\text{S}_3$  state to, for example, the dissociative  $^1\pi\sigma^*$  PES. The observed recoil anisotropy of the fastest  $\text{C}_6\text{H}_5\text{S}(\text{X}^2\text{B}_1)$  and  $\text{C}_6\text{H}_5\text{S}(\text{X}^2\text{B}_2)$  products indicates that such transfer must be fast and efficient, but the increased yield of slow H atoms in the measured spectra (Figures 4c and 10) points to alternative fragmentation channels also.

**Photolysis of  $\text{C}_6\text{H}_5\text{SD}$  and the Origin of the Slow H Atom Signal.** Analysis of TKER spectra derived from D atom TOF measurements following photolysis of  $\text{C}_6\text{H}_5\text{SD}$  in this same wavelength range provides some insights into these alternative fragmentation processes. The spectrum obtained by monitoring D atoms following excitation at  $\lambda_{\text{phot}} = 250.0$  nm (Figure 11a) shows two maxima, attributable to S–D bond fission on the  $^1\pi\sigma^*$  PES and formation of  $\text{C}_6\text{H}_5\text{S}$  products in their  $\text{X}^2\text{B}_1$  and  $^2\text{B}_2$  electronic states (as found when monitoring H atom products from  $\text{C}_6\text{H}_5\text{SH}$  photolysis at similar wavelengths), but the relative yield of slow products is greatly reduced. To assess the extent of deuteration in the  $\text{C}_6\text{H}_5\text{SD}$  sample, TOF spectra were also recorded at  $\lambda_{\text{phot}} = 243.136$  and 243.069 nm, wavelengths appropriate for two-photon  $2s \leftarrow 1s$  excitation of, respectively, any H and D atom products, without the presence of the Lyman- $\alpha$  probe laser pulse (or the 364.7 nm radiation from which it is derived). Any  $\text{H}^+/\text{D}^+$  ions formed by 2 + 1 REMPI at the  $\lambda_{\text{phot}}$  wavelength were promptly extracted by the 25 V  $\text{cm}^{-1}$  field that spans the interaction volume, but neutral H/D ( $n = 2$ ) atoms that avoided ionization were then excited with the  $\sim 366$  nm Rydberg tagging laser pulse and their TOFs detected in the usual manner. The TKER spectrum obtained at  $\lambda_{\text{phot}} = 243.069$  nm (Figure 11b, resonant with the  $2s \leftarrow 1s$  transition of D) is similar to that obtained at  $\lambda_{\text{phot}} = 250.0$  nm and can be interpreted accordingly. The spectrum obtained at  $\lambda_{\text{phot}} = 243.136$  nm (Figure 11c, resonant with the  $2s \leftarrow 1s$  transition of H) shows some signal at TKER  $\sim 12750$  and  $\sim 10000$   $\text{cm}^{-1}$ , attributable to formation of  $\text{H} + \text{C}_6\text{H}_5\text{S}(\text{X}^2\text{B}_1)$  and  $\text{H} + \text{C}_6\text{H}_5\text{S}(\text{X}^2\text{B}_2)$  products, implying the presence of some residual  $\text{C}_6\text{H}_5\text{SH}$  in the  $\text{C}_6\text{H}_5\text{SD}$  sample. More revealing, however, is the dominant feature at low TKER, which is barely evident in the corresponding spectrum obtained by monitoring D atom products (Figure 11b). The ratio of “fast” to “slow” H atoms in this spectrum is much smaller than that in the

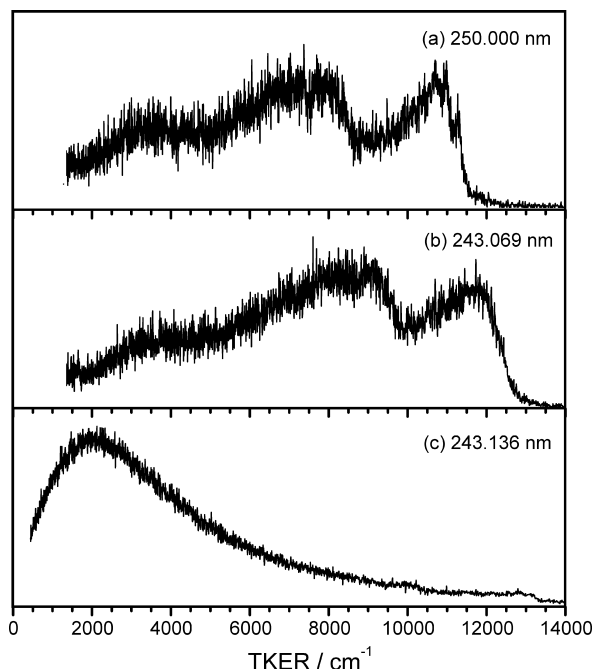


**Figure 11.** TKER spectra derived from D atom TOF spectra (with the assumption that all cofragments have the mass of  $\text{C}_6\text{H}_5\text{S}$ ) measured following photolysis of the  $\text{C}_6\text{H}_5\text{SD}$  sample at  $\lambda_{\text{phot}} =$  (a) 250.00 and (b) 243.069 nm, with  $\epsilon_{\text{phot}}$  aligned at  $\theta = 90^\circ$  to the TOF axis; (c) shows the corresponding TKER spectrum derived from H atom TOF spectra measured from the same  $\text{C}_6\text{H}_5\text{SD}$  sample (and any  $\text{C}_6\text{H}_5\text{SH}$  impurity it contained) at  $\lambda_{\text{phot}} = 243.136$  nm.

corresponding spectrum from  $\text{C}_6\text{H}_5\text{SH}$  (recall Figure 4c), confirming that most of this slow H atom signal must arise from  $\text{C}_6\text{H}_5\text{SD}$  dissociation. As commented previously, these slow products are most readily attributable to unimolecular decay of highly vibrationally excited parent molecules in their ground electronic state (formed by radiationless transfer following one- (or multi-) photon excitation). The preponderance of H rather than D atom products at low TKER hints at the operation of competing C–H bond fission processes in the statistical decay of such highly excited parents, but any fuller discussion of such decays must await more detailed knowledge of the ground-state PES, the molecular rearrangements that it can support prior to fragmentation, and the possible kinetic isotope effects that might discriminate against D atom loss.

#### 4. Conclusions

This translational spectroscopy study of the H(D) atom photofragments from  $\text{C}_6\text{H}_5\text{SH}(\text{C}_6\text{H}_5\text{SD})$  confirms S–H(S–D) bond fission as a primary dissociation process throughout the  $225 \leq \lambda_{\text{phot}} \leq 290$  nm wavelength range investigated. The partner  $\text{C}_6\text{H}_5\text{S}$  fragments are formed in both their ground ( $\text{X}^2\text{B}_1$ ) and first excited ( $^2\text{B}_2$ ) electronic states, in a spread of vibrational levels that broadens and shifts to higher  $E_{\text{int}}(\text{C}_6\text{H}_5\text{S})$  as  $\lambda_{\text{phot}}$  is reduced. Analysis of parent excitation spectra, of resolvable vibrational structure within the TKER spectra of the H(D) +  $\text{C}_6\text{H}_5\text{S}$  products, and of the recoil anisotropy of these fragments leads to the following conclusions. Excitation at  $\lambda_{\text{phot}} > 275$  nm results in population of quasi-bound levels of the  $^1\pi\pi^*(\text{S}_1)$  state, which decay by tunneling to the  $^1\pi\sigma^*$  PES. Torsional motion of the S–H group is identified as a likely coupling mode, facilitating population transfer at the CI between the diabatic  $^1\pi\pi^*$  and  $^1\pi\sigma^*$  PESs. Flux evolving on the  $^1\pi\sigma^*$  PES samples a second CI, at longer  $R_{\text{S–H}}$ , between the diabatic  $^1\pi\sigma^*$  and  $^1\pi\pi$  PESs, where the branching between ground- and excited-

state  $\text{C}_6\text{H}_5\text{S}$  fragment formation is established. The populated vibrational levels in each product channel have to satisfy symmetry conservation. All populated levels of  $\text{C}_6\text{H}_5\text{S}(\text{X}^2\text{B}_1)$  identified in the TKER spectra have  $a'$  vibrational symmetry; the in-plane modes identified as active can be understood in terms of vertical (and/or dynamic) Franck–Condon effects. The vibrational energy disposal within the  $\text{C}_6\text{H}_5\text{S}(\text{X}^2\text{B}_1)$  products is very different, involving levels with  $a''$  vibrational symmetry, particularly modes  $\nu_{11}$  and  $\nu_{16a}$ . As in phenol, the corresponding parent modes are deduced to promote coupling at the  ${}^1\pi\sigma^*/{}^1\pi\pi$  CI. Such detailed vibrational assignments allow new and improved determinations of the bond dissociation energies,  $D_0(\text{C}_6\text{H}_5\text{S}-\text{H}) = 28030 \pm 100 \text{ cm}^{-1}$  and  $D_0(\text{C}_6\text{H}_5\text{S}-\text{D}) = 28610 \pm 100 \text{ cm}^{-1}$ , and of the energy separation between the  $\text{X}^2\text{B}_1$  and  ${}^2\text{B}_2$  states of the  $\text{C}_6\text{H}_5\text{S}$  radical,  $T_{00} = 2800 \pm 40 \text{ cm}^{-1}$ .

Details of the energy disposal evolve as  $\lambda_{\text{phot}}$  is reduced. Once  $\lambda_{\text{phot}} \leq 275 \text{ nm}$ , the fastest  $\text{C}_6\text{H}_5\text{S}$  fragments in both product channels display anisotropic recoil velocity distributions, with a preference for  $\mathbf{v}$  being perpendicular to  $\boldsymbol{\epsilon}_{\text{phot}}$  and thus to the transition dipole moment. This finding is interpreted in terms of direct  $\text{S}_2 \leftarrow \text{S}_0(\sigma^* \leftarrow \pi)$  excitation and prompt dissociation on the  ${}^1\pi\sigma^*$  PES, with subsequent product branching determined by the  ${}^1\pi\sigma^*/{}^1\pi\pi$  CI, as seen at longer  $\lambda_{\text{phot}}$ .  $\text{S}_1 \leftarrow \text{S}_0(\pi^* \leftarrow \pi)$  excitation is also deduced to occur at these same wavelengths. Franck–Condon considerations require that the resulting  $\text{S}_1$  parent molecules are necessarily vibrationally excited but predominantly in “spectator” modes that are, at best, weakly coupled to the dissociation coordinate. Such molecules are deduced to dissociate by tunneling to the  ${}^1\pi\sigma^*$  PES in much the same way as that at longer  $\lambda_{\text{phot}}$ , with excitation in the “spectator” modes mapping through into the corresponding product vibrational levels. Not all of the excess energy is thus available for release as kinetic energy, and the formation of such products leads to a progressive broadening and loss of structure in TKER spectra measured at shorter  $\lambda_{\text{phot}}$ . Once  $\lambda_{\text{phot}} \leq 260 \text{ nm}$ ,  $\text{S}_3 \leftarrow \text{S}_0(\pi\pi^*)$  excitation dominates, but the observed energy disposal and the evident recoil anisotropy of the fastest  $\text{C}_6\text{H}_5\text{S}(\text{X}^2\text{B}_1)$  and  $\text{C}_6\text{H}_5\text{S}(\text{X}^2\text{B}_2)$  products indicates that coupling between the  $\text{S}_3$  and  ${}^1\pi\sigma^*$  states via one or more, as yet unknown, CIs must be both fast and efficient. The relative increase in the yield of slow H atoms following excitation at short  $\lambda_{\text{phot}}$  suggests that other fragmentation channels, most probably involving unimolecular decay of highly vibrationally excited ground-state molecules, also gain in importance.

The UV photochemistry of gas-phase thiophenol shows similarities with, but also a number of significant differences from, that of the first-row analogue, phenol. Both molecules dissociate by X–H bond fission following excitation at the respective  $\text{S}_1 \leftarrow \text{S}_0$  origins and at all shorter  $\lambda_{\text{phot}}$ . In both cases, the decay rate from low levels of the respective  $\text{S}_1$  states is sufficiently slow that the resulting H atoms show isotropic recoil velocity distributions. However, the lack of  $1 + 1$  REMPI signal via the  $\text{S}_1$  state of thiophenol and the widths of individual features in the action spectra for forming H(D) atoms following  $\text{S}_1 \leftarrow \text{S}_0$  excitation of  $\text{C}_6\text{H}_5\text{SH}(\text{C}_6\text{H}_5\text{SD})$  both indicate that the lifetime of thiophenol( $\text{S}_1$ ) molecules is much shorter than that of phenol( $\text{S}_1$ ) molecules at comparable levels of excitation. The reduced lifetime of thiophenol( $\text{S}_1$ ) molecules can be traced to improved coupling to the dissociative  ${}^1\pi\sigma^*$  state, the energy of which is lower in thiophenol (relative to that of the valence  ${}^1\pi\pi^*(\text{S}_1)$  state) than in phenol, mirroring the differences in parent ionization potential [8.30 eV (thiophenol),<sup>18</sup> 8.51 eV (phenol)<sup>33</sup>]. Photoexcited  $\text{C}_6\text{H}_5\text{SH}$  molecules are thus deduced to dissociate either by (torsionally mediated) tunneling to the

${}^1\pi\sigma^*$  PES via the  ${}^1\pi\pi^*/{}^1\pi\sigma^*$  CI and/or, once  $\lambda_{\text{phot}} \leq 275 \text{ nm}$ , following direct population of this  $\text{S}_2({}^1\pi\sigma^*)$  state. In either scenario, the dissociating flux samples the upper part of the subsequent  ${}^1\pi\sigma^*/{}^1\pi\pi$  CI at longer  $R_{\text{S-H}}$ , where the branching into specific vibrational levels of the ground ( $\text{X}^2\text{B}_1$ ) and first excited ( ${}^2\text{B}_2$ ) states of the  $\text{C}_6\text{H}_5\text{S}$  fragment is determined. Phenol( $\text{S}_1$ ) molecules, in contrast, are deduced to dissociate by internal conversion to vibrational levels of the ground state. Subsequent O–H stretching motion on the  ${}^1\pi\pi$  PES projects flux to the lower part of the  ${}^1\pi\pi/{}^1\pi\sigma^*$  CI and then to specific, symmetry allowed vibrational levels of the ground-state  $\text{C}_6\text{H}_5\text{O}$  radical. This alternative route through the  ${}^1\pi\pi/{}^1\pi\sigma^*$  CI, and/or the much greater energy separation between the  $\text{X}^2\text{B}_1$  and  ${}^2\text{B}_2$  states in  $\text{C}_6\text{H}_5\text{O}$ , apparently precludes formation of excited-state  $\text{C}_6\text{H}_5\text{O}$  radicals in  $\text{C}_6\text{H}_5\text{OH}$  photolysis at all UV wavelengths studied thus far.

**Acknowledgment.** The authors are extremely grateful to the EPSRC for financial support via the pilot portfolio partnership LASER and to Prof. J. N. Harvey, and to K. N. Rosser, and T. A. A. Oliver for their many and varied contributions to this work.

## Appendix 1

In the following table, B3LYP harmonic wavenumbers for the fundamental vibrational modes of  $\text{C}_6\text{H}_5\text{SH}$  in its ground state and for the  $\text{C}_6\text{H}_5\text{S}$  radical in its ground ( $\text{X}^2\text{B}_1$ ) and first excited ( ${}^2\text{B}_2$ ) electronic states, numbered as in phenol (ref. 5) using the Wilson mode labelling scheme and ordered on the basis of the  $C_{2v}$  symmetry labels of the radical products, are given. Anharmonic wavenumbers for these fundamental modes of vibration are listed for the respective ground states also.

C <sub>6</sub> H <sub>5</sub> SH (X <sup>1</sup> A')				C <sub>6</sub> H <sub>5</sub> S (X <sup>2</sup> B <sub>1</sub> )			C <sub>6</sub> H <sub>5</sub> S(X <sup>2</sup> B <sub>2</sub> )
mode	symmetry	harmonic	anharmonic	symmetry	harmonic	anharmonic	harmonic
20a	a'	3193	3045	a <sub>1</sub>	3199	3061	3203
2	a'	3176	3045	a <sub>1</sub>	3186	3060	3191
13	a'	3162	3083	a <sub>1</sub>	3165	3016	3171
S-H str	a'	2684	2472	disappearing mode			
8a	a'	1631	1587	a <sub>1</sub>	1599	1555	1596
19a	a'	1512	1480	a <sub>1</sub>	1482	1441	1488
9a	a'	1208	1188	a <sub>1</sub>	1200	1183	1201
7a	a'	1112	1082	a <sub>1</sub>	1079	1056	1081
18a	a'	1046	1028	a <sub>1</sub>	1039	1021	1040
1	a'	1015	1002	a <sub>1</sub>	1005	990	1007
S-H bend	a'	930	849	disappearing mode			
12	a'	706	697	a <sub>1</sub>	730	722	731
6a	a'	409	406	a <sub>1</sub>	428	425	427
20b	a'	3182	3060	b <sub>2</sub>	3196	3070	3200
7b	a'	3166	3032	b <sub>2</sub>	3175	3039	3180
8b	a'	1619	1578	b <sub>2</sub>	1579	1539	1578
19b	a'	1477	1446	b <sub>2</sub>	1461	1428	1465
14	a'	1354	1330	b <sub>2</sub>	1343	1329	1345
3	a'	1317	1276	b <sub>2</sub>	1303	1269	1299
9b	a'	1183	1168	b <sub>2</sub>	1181	1166	1181
15	a'	1106	1078	b <sub>2</sub>	1097	1086	1096
6b	a'	632	626	b <sub>2</sub>	621	614	623
18b	a'	277	263	b <sub>2</sub>	300	298	298
5	a''	970	967	a <sub>2</sub>	992	981	1003
10a	a''	838	833	a <sub>2</sub>	846	836	850
16a	a''	410	401	a <sub>2</sub>	386	380	387
17a	a''	996	984	b <sub>1</sub>	1011	992	1016
17b	a''	900	896	b <sub>1</sub>	941	928	952
10b	a''	744	741	b <sub>1</sub>	766	760	780
4	a''	702	696	b <sub>1</sub>	685	674	691
16b	a''	476	470	b <sub>1</sub>	463	458	470
11	a''	183	147	b <sub>1</sub>	160	157	161
τ <sub>S-H</sub>	a''	83		disappearing mode			

## References and Notes

- (1) Sobolewski, A. L.; Domcke, W. *Chem. Phys.* **2000**, 259, 181.
- (2) Ashfold, M. N. R.; Cronin, B.; Devine, A. L.; Dixon, R. N.; Nix, M. G. D. *Science* **2006**, 312, 1637.



- (3) Sobolewski, A. L.; Domcke, W.; Dedonder-Lardeux, C.; Jouvét, C. *Phys. Chem. Chem. Phys.* **2003**, 5, 315.
- (4) Lan, Z. G.; Domcke, W.; Vallet, V.; Sobolewski, A. L.; Mahapatra, S. *J. Chem. Phys.* **2005**, 122, 224315.
- (5) Nix, M. G. D.; Devine, A. L.; Cronin, B.; Dixon, R. N.; Ashfold, M. N. R. *J. Chem. Phys.* **2006**, 125, 133318.
- (6) Scott, D. W.; McCullough, J. P.; Hubbard, W. N.; Messerly, J. F.; Hossenlopp, I. A.; Frow, F. R.; Waddington, G. *J. Am. Chem. Soc.* **1956**, 78, 5463.
- (7) Remacle, F.; Kryachko, E. S. *J. Mol. Struct.* **2004**, 708, 165.
- (8) Larsen, N. W.; Nicolaisen, F. M. *J. Mol. Struct.* **1974**, 22, 29.
- (9) Nourbakhsh, S.; Yin, H.-M.; Liao, C.-L.; Ng, C. Y. *Chem. Phys. Lett.* **1992**, 190, 469.
- (10) Lim, J. S.; Lim, I. S.; Lee, K. S.; Ahn, D. S.; Lee, Y. S.; Kim, S. K. *Angew. Chem., Int. Ed.* **2006**, 45, 6290.
- (11) Lim, I. S.; Lim, J. S.; Lee, Y. S.; Kim, S. K. *J. Chem. Phys.* **2007**, 126, 034306.
- (12) Devine, A. L.; Nix, M. G. D.; Cronin, B.; Ashfold, M. N. R. *Phys. Chem. Chem. Phys.* **2007**, 9, 3749.
- (13) Cronin, B.; Nix, M. G. D.; Qadiri, R. H.; Ashfold, M. N. R. *Phys. Chem. Chem. Phys.* **2004**, 6, 5031, and references therein.
- (14) Wilson, S. H. S.; Howe, J. D.; Ashfold, M. N. R. *Mol. Phys.* **1996**, 88, 841.
- (15) Cook, P. A.; Langford, S. R.; Dixon, R. N.; Ashfold, M. N. R. *J. Chem. Phys.* **2001**, 114, 1672.
- (16) Huber, K.-P.; Herzberg, G. *Constants of Diatomic Molecules*; Van Nostrand Reinhold: New York, London, 1979.
- (17) Di Lonardo, G.; Zauli, C. *J. Chem. Soc. A* **1969**, 1305.
- (18) Faulk, J. D.; Dunbar, R. C.; Lifshitz, C. *J. Am. Chem. Soc.* **1990**, 112, 7893.
- (19) Hamprecht, F. A.; Cohen, A. J.; Tozer, D. J.; Handy, N. C. *J. Chem. Phys.* **1998**, 109, 6264.
- (20) Frisch, M. J.; Trucks, G. W.; Schlegel, H. B.; Scuseria, G. E.; Robb, M. A.; Cheeseman, J. R.; Montgomery, J. A., Jr.; Vreven, T.; Kudin, K. N.; Burant, J. C.; Millam, J. M.; Iyengar, S. S.; Tomasi, J.; Barone, V.; Mennucci, B.; Cossi, M.; Scalmani, G.; Rega, N.; Petersson, G. A.; Nakatsuji, H.; Hada, M.; Ehara, M.; Toyota, K.; Fukuda, R.; Hasegawa, J.; Ishida, M.; Nakajima, T.; Honda, Y.; Kitao, O.; Nakai, H.; Klene, M.; Li, X.; Knox, J. E.; Hratchian, H. P.; Cross, J. B.; Bakken, V.; Adamo, C.; Jaramillo, J.; Gomperts, R.; Stratmann, R. E.; Yazyev, O.; Austin, A. J.; Cammi, R.; Pomelli, C.; Ochterski, J. W.; Ayala, P. Y.; Morokuma, K.; Voth, G. A.; Salvador, P.; Dannenberg, J. J.; Zakrzewski, V. G.; Dapprich, S.; Daniels, A. D.; Strain, M. C.; Farkas, O.; Malick, D. K.; Rabuck, A. D.; Raghavachari, K.; Foresman, J. B.; Ortiz, J. V.; Cui, Q.; Baboul, A. G.; Clifford, S.; Cioslowski, J.; Stefanov, B. B.; Liu, G.; Liashenko, A.; Piskorz, P.; Komaromi, I.; Martin, R. L.; Fox, D. J.; Keith, T.; Al-Laham, M. A.; Peng, C. Y.; Nanayakkara, A.; Challacombe, M.; Gill, P. M. W.; Johnson, B.; Chen, W.; Wong, M. W.; Gonzalez, C.; Pople, J. A. *Gaussian 03*, revision B.04; Gaussian, Inc.: Pittsburgh, PA, 2003.
- (21) Wilson, E. B. *Phys. Rev.* **1934**, 45, 706.
- (22) McMillen, D. F.; Golden, D. M. *Annu. Rev. Phys. Chem.* **1982**, 33, 493.
- (23) Bordwell, F. G.; Cheng, J.-P.; Ji, G.-Z.; Satish, A. V.; Zhang, X. *J. Am. Chem. Soc.* **1991**, 113, 9790.
- (24) dos Santos, R. M. B.; Muralha, V. S. F.; Correia, C. F.; Guedes, R. C.; Cabral, B. J. C.; Simões, J. A. M. *J. Phys. Chem. A* **2002**, 106, 9883.
- (25) Dilabio, G. A.; Pratt, D. A.; LoFaro, A. D.; Wright, J. S. *J. Phys. Chem. A* **1999**, 103, 1653.
- (26) Fu, Y.; Lin, B.-L.; Song, K.-S.; Liu, L.; Guo, Q.-X. *J. Chem. Soc., Perkin Trans.2* **2002**, 1223.
- (27) Chandra, A. K.; Nam, P.-C.; Nguyen, M. T. *J. Phys. Chem. A* **2003**, 107, 9138.
- (28) Wright, J. S.; Rowley, C. N.; Chepelev, L. L. *Mol. Phys.* **2005**, 103, 815.
- (29) do Couto, P. C.; Cabral, B. J. C.; Simões, J. A. M. *Chem. Phys. Lett.* **2006**, 421, 504.
- (30) Cronin, B.; Devine, A. L.; Nix, M. G. D.; Ashfold, M. N. R. *Phys. Chem. Chem. Phys.* **2006**, 8, 3440.
- (31) Radziszewski, J. G.; Gil, M.; Gorski, A.; Spanget-Larsen, J.; Waluk, J.; Mroz, B. *J. J. Chem. Phys.* **2001**, 115, 9733.
- (32) Hause, M. L.; Yoon, Y. H.; Case A. S.; Crim, F. F. *J. Chem. Phys.* **2008**, 128, 104307.
- (33) Lipert, R. J.; Colson, S. D. *J. Chem. Phys.* **1990**, 92, 3240.